INFORMATION TO USERS

This manuscript has been reproduced from the microfilm master. UMI films the text directly from the original or copy submitted. Thus, some thesis and dissertation copies are in typewriter face, while others may be from any type of computer printer.

The quality of this reproduction is dependent upon the quality of the copy submitted. Broken or indistinct print, colored or poor quality illustrations and photographs, print bleedthrough, substandard margins, and improper alignment can adversely affect reproduction.

In the unlikely event that the author did not send UMI a complete manuscript and there are missing pages, these will be noted. Also, if unauthorized copyright material had to be removed, a note will indicate the deletion.

Oversize materials (e.g., maps, drawings, charts) are reproduced by sectioning the original, beginning at the upper left-hand corner and continuing from left to right in equal sections with small overlaps. Each original is also photographed in one exposure and is included in reduced form at the back of the book.

Photographs included in the original manuscript have been reproduced xerographically in this copy. Higher quality 6" x 9" black and white photographic prints are available for any photographs or illustrations appearing in this copy for an additional charge. Contact UMI directly to order.

U·M·I

University Microfilms International
A Bell & Howell Information Company
300 North Zeeb Road, Ann Arbor, MI 48106-1346 USA
313/761-4700 800/521-0600

Order Number 9218288

Electromodulation study of Fermi level pinning in semiconductors

Yin, Xiaoming, Ph.D.

City University of New York, 1992

U·M·I
300 N. Zeeb Rd.
Ann Arbor, MI 48106

17

ELECTROMODULATION STUDY OF FERMI LEVEL PINNING IN SEMICONDUCTORS

by

XIAOMING YIN

A dissertation submitted to the Graduate Faculty in Physics in partial fulfillment of the requirements for the degree of Doctor of Philosophy, The City University of New York

1992

This manuscript has been read and accepted by the Graduate Faculty in Physics in satisfaction of the dissertation requirement for the degree of Doctor of Philosophy.

1/14/92
Date

Prof. Fred H. Pollak
Chair of Examining Committee

1/14/92
Date

Prof. Joseph B. Krieger
Executive Officer

Prof. Pedro A. Montano/Brooklyn College

Prof. Frederick W. Smith/City College

Prof. Micha Tomkiewicz/Brooklyn College

Dr. Jerry M. Woodall/IBM Research Lab.

Supervisory Committee

The City University of New York

ABSTRACT

Electromodulation Study of Fermi Level Pinning in Semiconductors

by

Xiaoming Yin

Advisor: Professor Fred. H. Pollak

In this thesis we present a photoreflectance (PR) study of the Fermi level pinning (V_F) on (001) MBE grown GaAs with uniform electric field. Surface photovoltage (V_S) effects were evaluated as a function of temperature (77K < T < 450K), pump beam wavelength, W-metal coverage (in-situ) and light intensity. The dependence of the measured barrier height, V_B (= V_F - V_S) on T and light intensity P can be explained by a modified version of the theory of Hecht yielding values of V_F = 0.77 ± 0.02V for n-type GaAs and V_F = 0.75 ± 0.02V for p-type GaAs at 300K. This analysis also provides an experimental estimation of the densities of surface states on the GaAs surface. The influence of W-metal coverage (in-situ) is to increase the effective area of the surface states and hence to reduce the effect of V_S.

The PR measurements with different pump wavelengths allowed us to accurately determine the photo-induced current.

Using photoreflectance the effects of Ar^+ sputtering and thermal annealing on V_F on (001) n- and p-type GaAs were studied. The measurements were performed in-situ in an ultrahigh vacuum chamber. The effect of the sputtering was to move V_F from midgap to near the conduction band for both types of materials. Subsequent UHV annealing (350°C) and air exposure restored V_F its original midgap value. These observations have considerable implications for various models of Schottky barrier formation. This work also demonstrates the need to simultaneously measure both n- and p-type material in order to obtain unambiguous results.

The effects of environment on the determination of V_F were investigated. The air exposure tend to passivate the surface and hence increase the surface photovoltage effects.

We report a new contactless mode of electroreflectance (CER) which employs a capacitor-like system. We have measured the CER spectra at 300K from a number of materials including SI bulk GaAs and bulk $Hg_{0.8}Cd_{0.2}Te$. We demonstrate that CER can conveniently be used to determine the sign of the surface band bending in semiconductors and semiconductor structures. Results will be presented on n- and p-type bulk GaAs, semi-insulating GaAs, nominally undoped $In_{0.15}Ga_{0.85}As$ (p-type) and n- and p-type GaAs and InP structures with large, almost constant electric fields.

To My Wife and Parent

ACKNOWLEDGEMENT

I wish to express my deepest gratitude to Professor Fred H. Pollak, my thesis advisor, of Brooklyn College of CUNY for his invaluable guidance and constant encouragement throughout my study and research. His enthusiasm and creativity in exploring and understanding physics will always be my inspiration.

I also would like to express my sincere appreciation to the distinguished members of Supervisory Committee for their careful reading of this manuscript and their helpful advice, in particular, to Dr. Jerry M. Woodall of IBM, for his valuable advice and encouragement during the course of this work.

I greatly appreciate Mr. G.D. Pettit and Dr. D.T. McInturff of IBM for sample growth and preparation. I am grateful to Dr. P.D. Kirchner, A.C. Warren of IBM, Mr. Y. Cao, Mr. Y. Chan, Dr. E.G. Look, Mr. H. Qiang, Dr. W. Shen, Dr. D. Yan and Mr. Y. Yin of Physics Department of Brooklyn College. Special thanks to Ms H-M. Chen and Ms. X. Guo for their team spirit and corporation. Finally special thanks to my wife for her devoted support and patient sacrifice during the course of this work.

Xiaoming Yin

Brooklyn, New York

Jan., 1992

CONTENTS

INTRODUCTION 1

Chapter I: REVIEW OF VARIOUS MODELS OF
SCHOTTKY BARRIER FORMATION 9

Work Function Models 9

Ideal Case: Schottky-Mott Theory of
Metal-Semiconductor Contacts 9

Non-Ideal Case: Effective Work
Function Model 13

Bardeen's Fermi Level Pinning Model 18

Intrinsic Surface States 21

Metal-Induced Gap States 22

Advanced Unified Defect Model 24

Other Extrinsic Trap States 27

Chapter II: MODULATION SPECTROSCOPY 29

Principle and Technique of
Modulation Spectroscopy 29

Lineshape Consideration of
Electromodulation.................................. 32

Third Derivative Spectroscopy
(Low-Field Regime) 33

Franz-Keldysh Oscillations
(Intermediate Field Regime) 36
First Derivative Spectroscopy 45
UN^+ (UP^+) Structure 47
Experimental Techniques 51
Photoreflectance 51
New Contactless Mode
of Electroreflectance 55

Chapter III: EXPERIMENTAL RESULTS 62

Surface Photovoltage Effects 64
In-situ Photoreflectance Study of the
Effects of Sputter/Annealing on the Fermi
Level at (001) n- and p-type
GaAs Surfaces 78
Experimental Details and Results 79
Discussion 82
Evolution of the Surface Voltage of Air
Exposed MBE-grown (001) GaAs 84
Nature of Band Bending at Semiconductor
Surfaces by Contactless
Electroreflectance 87
A Electromodulation Study of GaAs
with Excess Arsenic 95

Chapter IV: SUMMARY AND CONCLUSIONS 96

APPENDIX: PUBLICATIONS 101

BIBLIOGRAPHY 104

LIST OF TABLES

Table I. III-V oxide reactions 16

Table II. Fit results of Fig. 19 75

Table III. Measured barrier height for both in UHV and in air. 86

LIST OF FIGURES

Figure 1. Electron energy band diagrams of metal contact to n-type semiconductor with $\phi_m > \phi_{ns}$ (a) Neutral materials separated from each other and (b) thermal equilibrium situation after the contact has been made 11

Figure 2. Schematic diagram illustrating principles of the EWF model. ϕ_{M1}, ϕ_V, ϕ_{M2} are arbitarily chosen to demonstrate the effect, ϕ_{eff} appropriately average the effects of the various interface phases 14

Figure 3. Interface Fermi level for relatively unreactive (mostly Au) contacts to various III-V compounds and alloys. On an absolute energy scale, the Fermi level "pinning" energies lie within the band gaps at the anion work function energy 17

Figure 4. Electron energy band diagrams of n-type semiconductor with surface states. The diagrams show (a) flat band at surface,

(b) surface in thermal equilibrium with the bulk, and (c) semiconductor in contact with a metal 19

Figure 5. Localized wavefunction tunneling (a) into both vacuum and the semiconductor band gap at a semiconductor surface and (b) into the semiconductor band gap at a metal-semiconductor interface. The exponentially decaying behavior leads to a continuous density of intensity of interface states shown in (c) (after F. Flores and C. Tejedor, Ref. 60) for a one-dimensional model of a covalent semiconductor-metal interface 23

Figure 6. The diagram to the left is taken from Ref. 12. This energy level diagram indicates the pinning positions measured by XPS on n- and p-type GaAs (110) surfaces with very low coverages (order 1ML or less) of the indicated element at room temperature (Eg-1.42eV). The relatively constant energies for different adsorbates suggest that native defects (i.e., antisite defects) associated with the semiconductor rather than the adatom are responsible for pinning the Fermi level. The right

diagram indicates the energy of the As_{Ga} antisite levels from the valence band maximum measured at 8K (E_g=1.52eV) by Weber et al. [Ref. 61] 25

Figure 7. Plots of (a) $\varepsilon_2(E-E_g,F)$ and $\varepsilon2(E-E_g,0)$ from Eq. (17) and (b) $\Delta\varepsilon_2(\eta)$ from Eq. (18). 40

Figure 8. The electro-optic functions $G(\eta)$ and $F(\eta)$ for different values of the broadening parameter Γ (in units of $h\theta$) (after Shen and Pollak Ref.74) 42

Figure 9. Schematic representation of the band structures of (a) UN^+ and (b) UP^+ configurations for buffer doping levels of $2 \times 10^{18}cm^{-3}$ for the UN^+ sample and $1 \times 10^{18}cm^{-3}$ for the UP^+ sample. The influence of light on the barrier height is shown. 48

Figure 10. Photoreflectance spectrum of the UN^+ sample at room temperature with P_{pu} = $3\mu W\text{-}cm^{-2}$ (633nm line) and P_{pr} = $2\mu W\text{-}cm^{-2}$. The inset shows a

plot of $(4/3\pi)(E_n-E_o)^{3/2}$ as a function
of FKO index n. 51
Figure 11. Schematic function block diagram of
photoreflectance set up. 54
Figure 12. Schematic function block diagram of
CER set up. 57
Figure 13. Schematic view of the condenser-like
arrangement used in CER system 58
Figure 14. The CER and PR spectra of bulk semi-
insulating GaAs at 300K. The dotted
lines are a least-squares fits for a FDGL 59
Figure 15. The CER spectrum of bulk $Hg_{0.8}Cd_{0.2}Te$
at 300K. The dotted line is a least-
squares fit to a TDFF for a two-
dimensional critical point. 60
Figure 16. PR spectrum of the UN^+ sample at 300K
(P_{pr} = 2 μW-cm^{-2}) with pump wavelengths
of 633 nm (dashed curve) and 407 nm (solid
curve). Both of the pump beams had a photon
flux of 2 x 10^{13} photons-s^{-1}cm^{-2}. 65
Figure 17. The measured barrier height V_B of the
UN^+ (triangles) and the UP^+ (squares)
samples as a function of temperature
with P_{pu}=3μW-cm^{-2} (633nm line) and

$P_{pr}=2\mu W\text{-}cm^{-2}$. The solid ($UN^+$) and dashed ($UP^+$) lines are least-squares fits to Eq. (29). The obtained values of $V_F(300)$, r and η are shown in the inset. $V_F(300)$ is in units of volts. The dot-dashed line is a least-squares fit (UN^+) to Eq.(29) for r = 1. 66

Figure 18. Values of V_B of the UN^+ sample in an ultra-high vacuum chamber, before and after 4 monolayer of W deposition, as a function of temperature with $P_{pu} = 40\mu W\text{-}cm^{-2}$ (633nm line) and $P_{pr} = 10\mu W\text{-}cm^{-2}$. The solid (before evaporation) and dashed (after evaporation) lines are least-squares fits to Eq. (29). The obtained values of $V_F(300)$, r and η are shown in the inset. $V_F(300)$ is in units of volts 67

Figure 19. Measured barrier height V_B of the UN^+ sample as a function of temperature and light intensity. The solid lines are least-squares fits to Eq. (29). The dashed line is a generated curve corresponding to

a light intensity of $0.4\mu W\text{-}cm^{-2}$ 69

Figure 20. The measured barrier height V_B of the UN^+ (squares) and UP^+ (circles) samples as a function of Ar^+ sputtering time, thermal annealing and air exposure. the triangles are the sum of $V_B(n)+V_B(p)$. The band gap of GaAs, E_g = 1.42eV, also is denoted. 81

Figure 21. Photoreflectance spectra in MBE chamber and after exposure to air. 86

Figure 22. $(4/3\pi)(E_m-E_o)^{3/2}$ as a function of index m. 86

Figure 23. Contactless electroreflectance spectra at 300K in the region of E_o from p-type GaAs (solid line), n-type GaAs (dotted line), SI GaAs (dashed line) and nominally undoped $In_{0.15}Ga_{0.85}As$ (dot-dashed line). 90

Figure 24. Contactless electroreflectance spectra at 300K in the region of E_1 from p-type GaAs (solid line), n-type GaAs (dotted line) and SI GaAs (dashed line) 91

Figure 25. Contactless electroreflectance spectra at 300K in the region of E_o and E_1 transitions from UP^+ and UN^+ GaAs

structures. 92

Figure 26. Contactless electroreflectance spectra at 300K in the region of E_o and E_1, $E_1 + \Delta_1$ transitions from UP$^+$ and UH$^+$ InP structures. 93

INTRODUCTION

Fermi level pinning at semiconductor surfaces and interfaces is a challenging subject of investigation from both fundamental and applications-oriented points of view [1-4]. There exists at many semiconductor surfaces/interfaces an appreciable density of uncontrolled electronic states, whose origin is still a topic of controversy. These states tend to "fix" the location of the Fermi level at these surfaces/interfaces at some characteristic energy (V_F). Fermi level pinning behavior has been observed at the free surface, oxide interface, metal interface (Schottky barrier), MBE grown surface, stop-regrown homojunction and misfit-dislocation pinned heterojunctions of various semiconductors. This pinning adversely affects the performance of both high speed and optoelectronic devices and integrate circuits. The lack of understanding and solution still hampers the development of compound semiconductor devices.

Fermi level pinning is manifest in several ways. One of the most notable is the insensitivity of the Schottky barrier height (SBH) to the metal work function [1-5]. Despite decades of intense study on metal-semiconductor contacts, the enigma of Schottky-barrier formation still challenges basic solid state research. W. Schottky [6], provided perhaps the simplest model for this phenomenon, namely the band bending within the semiconductor is the difference of the work

functions of the metal and semiconductor. This model did not account for the relative insensitivity of the SBH on metal work function and the deviations were explained by Bardeen in terms of semiconductor surface (or interface) states [7]. In this approach, the Fermi level is pinned in the semiconductor band gap by electronic states, so that the SBH for n-type (p-type) semiconductor is equal to the energetic depth of the pinning states below (above) the conduction band edge (the valence band edge).

The origin and nature of these surface/interface states still remain somewhat of a mystery; Hampering efforts to identify the physical mechanisms responsible for this Fermi level pinning has been the narrow ranges of reported Fermi stabilization energies themselves, which permit a number of quite dissimilar explanations. These pinning theories can be classified into two groups, (a) Fermi level pinning as an intrinsic property of the semiconductor related to either bulk or surface band structure, e.g. metal-induced gap states (MIGS) [8-10] (or some variant) [11], or (b) pinning as an extrinsic property of the semiconductor related to native [12] or antisite (at or near the surface) defects [13] or anion phase work function [14]. The diversity of models and invoked assumptions can be explained by the lack of precise experimental results on Fermi level pinning measured on a great variety of different types of non-ideal metal/semiconductor interfaces. A detailed explanation of various models will be given in Chapter I of this thesis.

For bulk semiconductor the equilibrium of the Fermi level in the bulk and at the surface is established through the formation of a depletion layer and the bending of the electronic bands within this layer. The Therefore, the Fermi level position at the surface cannot simply be derived from its bulk value but has to be measured separately for each surface, each of which may differ by crystallographic orientation [15] and reconstruction [16], surface chemistry or environment [1,17]. It seems certain that the location of the surface Fermi level depends strongly on the microscopic structure of non-ideal surfaces/interfaces. Also some of the reported results on SBH are measurements dependent. Thus, we might suspect that in order to make further progress in understanding Schottky barriers and/or the Fermi level pinning effects we need a versatile tool which can accurately measure V_F in a variety of ambients and semiconductor interfaces e.g. vacuum, air, metal/semiconductor, or semiconductor/semiconductor interfaces, etc. With such a tool, one could monitor changes in V_F over a wide range of experimental conditions. This in turn could produce strong inferences concerning the fundamental mechanisms which determine V_F in a wide variety of non-ideal interfaces.

In the past, the main experimental method to study Fermi level pinning at the semiconductor surface/interface has been soft X-ray photoemission (SXPS) [1-4,15]. However, as recently pointed out by Hecht [18] and confirmed by several groups [4,19,20], surface photovoltage (V_S) effects in SXPS

are an important factor. The measured barrier height V_B is thus the difference between V_F and V_S, i.e., $V_B = V_F - V_S$. Also since in SXPS the photoelectron escape depth is normally on the order of 1 to 2nm at most, the photoemission techniques cannot be used on buried interfaces. Other techniques to evaluate Fermi level pinning include the electromodulation method of photoreflectance (PR) [21-27], Raman scattering [17,28], photoluminescence [29], internal photoemission [30] and device measurements such as C-V profiling [1,5]. However, the latter two methods require contacts and hence cannot be performed on the free surface. Photoluminescence cannot be performed over wide temperature range. Although Raman scattering has been used to get information on Fermi level pinning effects, it is an indirect method and requires high light levels. Hence its use is very limited.

Electromodulation method (EM) such as PR is of considerable interest and usefulness since it is contactless, employs very low light levels, requires no special mounting of the sample, and can be performed in any transparent ambient including ultra high vacuum (UHV) [25,26,31,32]. From the Franz-Keldysh oscillations (FKO) [21-27] observed in EM spectra the built-in electric field and hence V_B can be accurately determined. The measured barrier height (V_B) is V_F minus any surface photovoltage (V_S) effects, i.e., $V_B = V_F - V_S$. Information about charge transfer mechanism at the surface/interface also can be obtained [25,27] since PR is the optical response of the system to the modulating field

[33] and it can be performed over a wide temperature range. In spite of the low light levels employed the influence of V_S also must be considered in the PR determination of V_F [24-27]. Also we recently have developed a novel contactless mode of electroreflectance (CER) which utilizes a condenser-like system and is a complement of PR [34]. The combination of PR and CER provides one more dimension to study surface/interface Fermi level pinning effects of semiconductors.

It has recently been demonstrated that special structures (designated as UN^+ and UP^+) which exhibit a large number of FKO can be used to accurately determine V_B and hence V_F [24-27,35,36]. These structures are made by fabricating an undoped layer of thickness L (~100nm) on a buried n^+ (p^+) buffer (n or p ~ $1x10^{18}cm^{-3}$) on an n^+ (P^+) substrates. Because of Fermi level pinning at the surface there is a large, almost constant electric field F in the undoped region between the buried n^+ (p^+) layer and the surface. Thus, these structures will exhibit a large number of FKO in because of the high field and small broadening parameter in the undoped region. The field F, as directly measured by the FKO, can easily related to surface Fermi level pinning effects [24-27,35].

In this thesis we have used PR to study the surface barrier height on (001) MBE grown GaAs under a variety of

conditions including air, ultrahigh-vacuum (UHV), sputter/annealing (in UHV), temperature (77K<T<450K) in air and UHV, etc. Surface photovoltage (V_S) effects were evaluated as a function of temperature (77K<T<450K), pump beam wavelength (633nm and 407nm), W-metal coverage (in-situ), and light intensity. The effects of Ar^+ sputtering (500V) and thermal annealing (350°C) on V_F were studied in-situ in an UHV chamber. Subsequent air exposure effects were also examined. The sample surfaces were monitored with Auger electron spectroscopy (AES) and high resolution low energy electron diffraction (LEED). In addition, the surface/interface Fermi level pinning effects have been investigated on (001) MBE grown low substrate growth temperature As-rich GaAs(GaAs:As) using PR as well as CER. The implication of our results for various models of Schottky barrier formation will be discussed. The need to simultaneously measure both n- and p-type material in order to obtain unambiguous results also was demonstrated.

The (001) surface of III-V compound semiconductors, such as GaAs, is the most technological important since it is the one upon which most epitaxial growth is performed for device applications. A wide variety of complex surface phenomena driven by changes in the surface stoichiometry characterize the GaAs (001) surface [37,38]. Two general regimes of the reconstructions of this surface exist which fall into As-rich and Ga-rich classes [37,39]. In addition, GaAs, by virtue of

its electronic properties, has an advantage over other semiconductors. Although during the past few years there has been extensive research on GaAs surfaces/interfaces, in contrast to Si, our understanding and technology of GaAs Schottky barrier are still far from complete. This is perhaps due to the fact that their behavior is highly process/measurement dependent.

Considerable work has demonstrated that departures from stoichiometry at surface/interface can affect the Fermi level position [14,40,41]. The explanations to these behaviors have been ambiguous [1-3]. The previous results can not distinguish between electronic effects due to introduction of native defects based on changes in atomic composition versus the changes in atomic composition themselves. In particular, the presence of excess anion (As) at III-V compound semiconductor surfaces/interfaces (GaAs) can stabilize the Fermi level due to the As work function or due to the formation of additional native defects which are sensitive to an As excess - for example, As antisite defects. Recently GaAs:As has attracted considerable attention for its technological applications. It has been shown that in GaAs:As without annealing exists huge amount of As antisite (As_{Ga}) defects, and with annealing at 600°C there is no detectable antisite defect signal [43]. In the latter case excess As is in the form of metal clusters [44]. Thus, examining these surfaces/interfaces may shed light on the importance of As-

related surface/interface effects.

Our work demonstrates the considerable utility of PR for both the study of environment on the electronic properties of semiconductor surfaces and for a better understanding of the charge transfer process.

The thesis is divided into three chapters. The first chapter reviews various models for Fermi level pinning effects. This part encompasses some of the very poorly understood problems in solid-states physics. A good overview of prior work can be obtained from a number of books and articles [1-4,45-48].

Chapter II deals with modulation spectroscopy. A brief theoretical background, especially FKO theory, for understanding our experiment results are given. The sample structures used and their advantages will be explained. In the experimental section we will focus on the PR and CER techniques.

Our experiment results are presented in Chapter III. A modified photovoltage expression of M. Hecht [18] will be presented.

In the last chapter we summarize our results and conclusions.

CHAPTER I

REVIEW OF VARIOUS MODELS OF SCHOTTKY BARRIER FORMATION

Over the past several decades, a common theme of metal-semiconductor interface studies has been the insensitivity of semiconductor band bending to the properties of different metal overlayers and physical mechanisms responsible for this Fermi level pinning. In the last several years there has been an eruption of new models for the mechanism of Schottky barrier formation based on some new experimental data [10,12,14,48]. Most of these models can be traced back to the foundations laid by Schottky [6] or Bardeen [7] many years ago.

This introductory chapter is devoted to the basic physics of some models of Schottky barrier formation. These models will be classified into two groups. One group does not invoke surface states, e.g., Schottky-Mott theory, EWF model etc. The other group, in the spirit of Bardeen, centers around the nature and source of the surface pinning states.

I. Work Function Models

A. Ideal Case: Schottky-Mott Theory of Metal-Semiconductor Contacts

The potential barrier, which forms when a semiconductor is contacted with a metal, arises from the separation of

charges at the metal-semiconductor interface such that a high-resistance region devoid of mobile carriers is created in the semiconductor. The earliest model to explain the barrier height is given by Schottky and Mott. According to this model the barrier results from the difference in the work functions of the two single phase substances. The energy diagrams in Fig. 1 illustrate the the process of barrier formation (for n-type semiconductor). Figure 1a shows the electron energy band diagram of a metal of work function ϕ_m and an n-type semiconductor of work function ϕ_{ns} which is smaller than ϕ_m. The work function of a metal is defined as the amount of energy required to raise an electron from the Fermi level to the vacuum level. The vacuum level is the energy level of an electron just outside the metal with zero kinetic energy and is the reference level in Fig. 1a. The work function ϕ_m has a volume contribution due to the periodic potential of the crystal lattice and a surface contribution due to the possible existence of a dipole layer at the surface. The work function ϕ_{ns} of semiconductor is defined similarly and is a variable quantity because the Fermi level in semiconductor varies with the doping. An important surface parameter which does not depend on doping is the electron affinity χ_s defined as the energy difference of an electron between the vacuum level and the conduction band minima. Note that the semiconductor shown in Fig. 1a

does not contain any charges at the surface (ideal surface) so that the band structure of the surface is the same as that

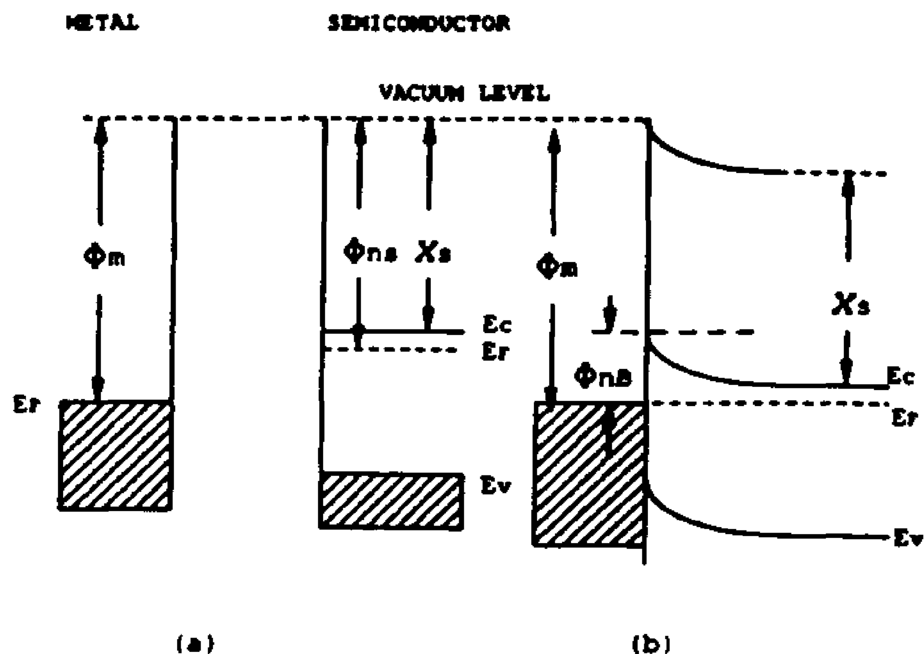

Figure 1. Electron energy band diagrams of metal contact to n-type semiconductor with $\phi_m > \phi_{ns}$ (a) Neutral materials separated from each other and (b) thermal equilibrium situation after the contact has been made.

of the bulk and there is no band bending. This is the case for the (110) cleavage face of some compound semiconductors where there are almost no surface steps and no surface states in the band gap [1,49-51]. Figure 1b shows the energy band

diagram after the contact is made and equilibrium has been reached. The conduction band electrons which cross over into the metal leave a positive charge of ionized donors behind, so the semiconductor region near the metal gets depleted of free electrons. Thus a depletion region is established on the semiconductor side of the interface and the electrons which cross over into the metal form a thin sheet of negative charge contained within the Thomas-Fermi screening distance from the interface (≈0.05-0.1nm). Since the vacuum level must remain continuous across the interface transition region then the barrier height ϕ_{nB} looking from the metal towards the semiconductor is given by:

$$\phi_{nB} = \phi_m - \chi_s \qquad (1)$$

Eq. (1) was stated by Schottky [6] and independently by Mott [52]. The exact shape of the barrier can be calculated from the donor distribution in the semiconductor. Schottky [6] assumed the semiconductor to be uniformly doped up to the metal interface, which gives rise to a uniform density in the depletion region. The electric field strength for this constant space charge increases linearly with distance from the edge of the space charge layer and the resulting parabolic barrier is known as a Schottky barrier. Mott [52] assumed a thin layer of semiconductor, devoid of any charge, sandwiched between a uniformly doped semiconductor and metal.

The electric field strength in the thin region is constant and the potential increases linearly across this region. This type of barrier is known as Mott barrier. The Mott barrier is encountered in situations where a thin layer of undoped, nearly intrinsic semiconductor (or oxide) is interposed between a metal and a heavily doped semiconductor.

In obtaining Eq. (1), it has been assumed that the surface dipole contributions to ϕ_m and ϕ_{ns} remain unchanged after the metal makes contact with the semiconductor. Note when $\phi_m \leq \chi_s$, i.e. $\phi_{nB} \leq 0$, an ideal ohmic metal-n-type-semiconductor contact is obtained. Likewise, when $\phi_m \geq \chi_s$, i.e. $\phi_{nB} \geq 0$, a rectifying contact is obtained. Thus, for the ideal case and for a given semiconductor, ϕ_{nB} should be determined by the metal work function. Unfortunately, this is not the case for GaAs and many semiconductors.

B. Non-Ideal Case: Effective Work Function Model

The interaction between metal and semiconductor can produce new interfacial phases and these can have effective work functions unlike that of the bulk metal. For metal interfaces with III-V compound semiconductors, a variety of techniques frequently reveal the presence of excess anions, especially As, segregated to the intimate junction. Freeouf and Woodall have suggested a new model (EWF model) which assumes that, at pinned interfaces, the interface Fermi level

location is determined by the work function of the anion released from the substrate by the processes used to generated the interface [14]. This behavior is shown in Fig. 2. The UHV cleaved (110) surface is free of intrinsic surface states and hence E_F is uniform as seen in Fig. 1a. All other

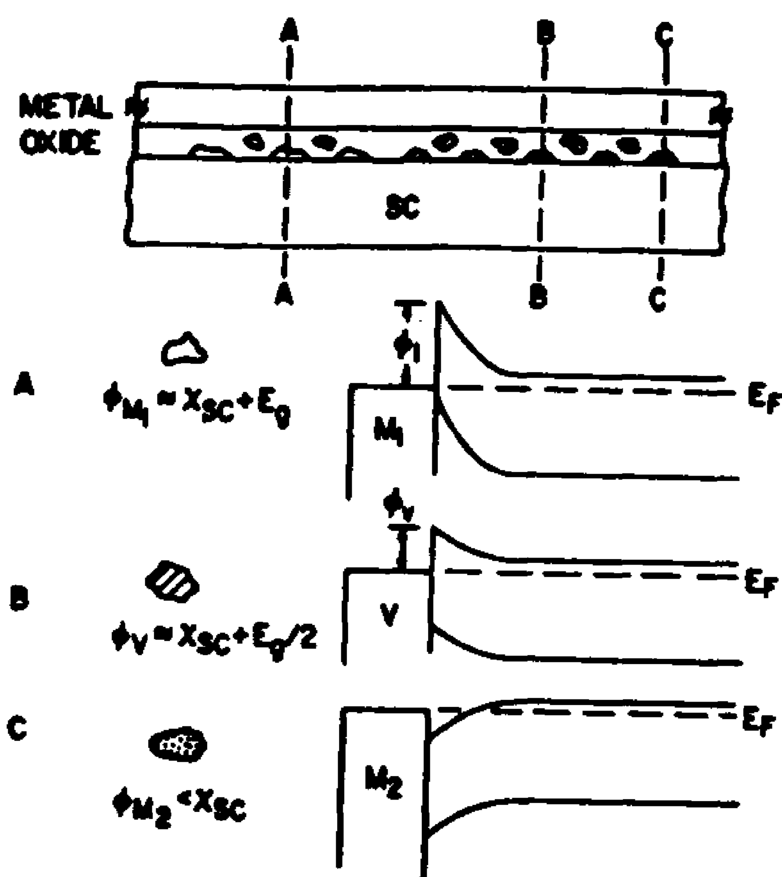

Figure 2. Schematic diagram illustrating principles of EWF model. ϕ_{M1}, ϕ_V, ϕ_{M2} are arbitrarily chosen to demonstrate the effect, ϕ_{eff} appropriately average the effects of the various interface phases.

surfaces exhibit band bending prior to any intentional environment. When a metal is deposited, there is a region at the interface which contains a matrix of native oxide embedded with microclusters of different phases, each having its own work function. Since the model does not require surface states, Eq.(1) can be modified and rewritten as [14,46]:

$$\phi_{nB} = \phi_{eff} - \chi_s \qquad (2)$$

where ϕ_{eff} is an appropriately weighted average of the work functions of the different interface phases. Thus, the measured ϕ_{nB} can depend somewhat on the measurement technique, i.e. C-V or I-V. In other words, the interface phases comprise the Schottky barrier contact. The rest of the bulk metallurgy has little or no effect on the barrier height, except when the interface phases are predominantly the same as the applied metallurgy.

For most III-V compounds, conventional metallization, i.e. non-UHV conditions, ϕ_{eff} in Eq. (2) is mainly due to ϕ_V, the work function of group V component which is generated by either one or both of the following reactions:

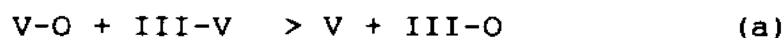

V-O + III-V > V + III-O (a)

M + III-V > (V, MV_x) + (M,III) (b)

where V-O and III-O are generic group V and III oxides and M is a metal.

TABLE I

III-V Oxide Reactions

	ΔF
AlP	(-) Large
GaP**	(+) Small
InP***	(~) 0
AlAs	(-) Large
GaAs*	(-) Large
InAs*	(-) Large
AlSb	(-) Large
GaSb	(-) Large
InSb	(-) Small
$Ga_{1-x}Al_xAs$*	(-) Large

* Excess V observed at interface
** Excess V not observed at interface
***Excess P observed, 350-550C anneal

The conditions for driving the reaction (a) to the right and hence generating excess V at the interface is that the Gibbs free energy, ΔF, is negative. A list such oxide

reactions is shown in Table 1 [14,46]. Note that excess group V has been experimentally observed when ΔF is negative, i.e. GaAs, InAs, InSb [53,54] and that is not observed when ΔF is positive, i.e. for GaP [54]. For GaAs, excess arsenic is usually observed at interface of MOSFET structures which have high interface state densities (10^{13} - 10^{14} cm^{-2}) [55]. The EWF model suggests the excess arsenic at the interface will form a positive Schottky barrier of 0.8 eV to GaAs which acts

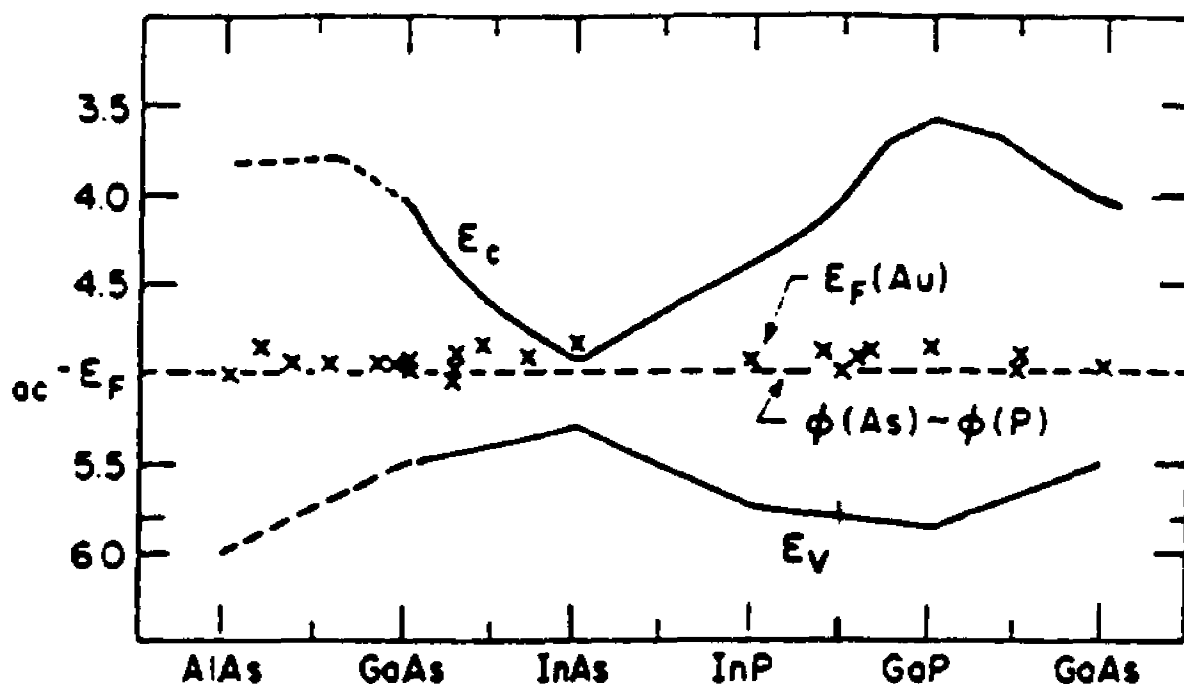

Figure 3. Interface Fermi level for relatively unreactive (mostly Au) contacts to various III-V compounds and alloys. On an absolute energy scale, the Fermi level "pinning" energies lie within the band gaps at the anion work function energy (after J.L. Freeouf and J.M. Woodall, Ref. 14).

like an interface state within the band gap. In addition to oxide reactions, excess group V can be generated by reaction of metals via reaction (b). For example, it is known that Au deposited on GaAs and GaP results in dissolved Ga in the Au film [56]. Also preliminary data [46] shows that an arsenic phase is expected at equilibrium for Au-GaAs and Au-InSb. Thus, a knowledge of both oxide and reactive metal chemistry should enable accurate predictions of the Schottky barrier heights for metal-III-V interfaces.

Another implication of the EWF model is that the observed pinning position should have a work function ($\phi = \phi_{nB} + \chi_s$) equal to that of the anion. Figure 3 illustrates the interface Fermi level location for some materials [14,57]. The conduction and valence bands for different semiconductors appear on an absolute energy scale. The Fermi level positions all fall at approximately the same energy, corresponding to a work function of 4.8-5.1 eV, close to the work functions of As and P.

II. Bardeen's Fermi Level Pinning Model

For practical metal-semiconductor contacts only in predominantly ionic semiconductors the dependence of barrier height on ϕ_m is observed. The insensitivity of barrier height to metal work function in covalently bonded semiconductors was first explained by Bardeen [7], who introduced the concept of Fermi level pinning due to surface or interface

states, an additional charge trapped there would screen the potential difference between metal and semiconductor.

In order to illustrate how the Fermi level can be pinned by surface states let us assume that surface states do exist in the forbidden gap, whatever their origin, and at least some of them are capable of acting as electron traps on n-type semiconductor. These surface states can be characterized by a neutral level ϕ_0. The position of this neutral level is such that when there is no band bending in the semiconductor

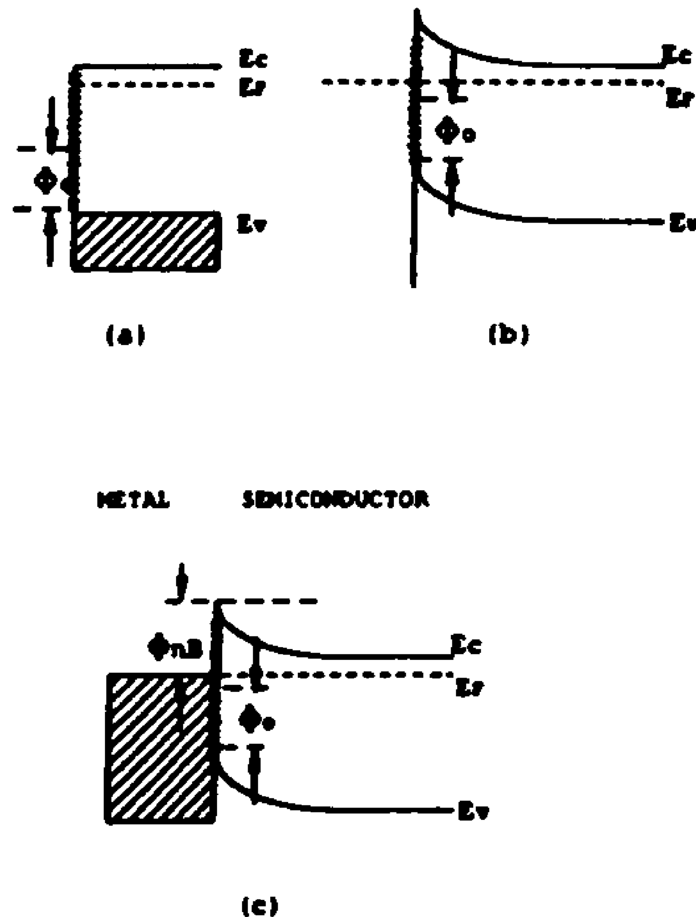

Figure 4. Electron energy band diagrams of n-type semiconductor with surface states. The diagrams show (a) flat band at surface, (b) surface in thermal equilibrium with the bulk, and (c) semiconductor in contact with a metal.

the states are occupied by electrons up to ϕ_0 making the surface neutral. The states below ϕ_0 are donorlike since they are neutral when occupied and are positive when empty. Obviously the states above ϕ_0 behave as acceptorlike.

Figure 4a shows the electron energy band diagram of an n-type semiconductor under flat band condition. This situation is a nonequilibrium. When equilibrium is reached the surface becomes negatively charged and a depletion layer consisting of ionized donors is formed in the semiconductor near the surface region. Because of this dipole formation a potential barrier looking from the surface towards the semiconductor is obtained even in the absence of a metal contact as shown in Fig. 4b. Of course, the barrier thickness depends on the donor concentration, as well as the barrier height, this, in turn, depends on the energetic position and number of surface states. When a metal is now brought in contact with the semiconductor and equilibrium is reached, the Fermi level in the semiconductor must change by an amount equal to the contact potential due to exchanging charge with the metal. If the density of surface states at semiconductor surface is very large ($>10^{12}$ - $10^{13} cm^{-2}$) then the charge exchange takes place largely between the metal and the surface states, i.e., such a surface state density will completely screen the semiconductor from the contact potential ($=\phi_m - \chi_s$). Thus the space charge region in the

semiconductor remains almost unaffected. As a result the barrier height in Fig. 4c becomes independent of the metal work function and is given by :

$$\phi_{nB} = E_g - \phi_0 \qquad (3)$$

In this case the barrier is said to be "pinned" by surface states. In the absence of additional complications, this must be true for p-type material. Pinned Fermi levels therefore imply $\phi_{nB} + \phi_{pB} = E_g$.

Trapped charge at interfaces can arise from several sources. The attempt to identify the microscopic nature of these pinning skates has generated the following sections of Fermi level pinning models.

A. Intrinsic Surface States

At the surface of a semiconductor the periodicity of the crystal lattice is terminated. In a covalent crystal each of the surface atoms has one broken covalent bond in which only one electron is present and the other is missing. This dangling bond give rise to a localized energy state at the surface of the semiconductor. An alternative way of looking at this problem is that the perturbation of vacuum level to the periodical crystal potential at surface will generate localized states (Tamm states) [58]. Before the 1970's these surface states were thought to be the dominant physics

responsible for the Fermi level pinning. With the development of UHV technology in the 1970's, extensive research on clean semiconductor surfaces revealed that in general such states did not exist in the semiconductor band gap. In fact, upon relaxation of the semiconductor surface atoms, energetically favorable bond angles and bond lengths will move the dangling bond states out of the band gap [59]. Thus intrinsic surface states do not play a significant role in barrier formation.

B. Metal-Induced Gap States

When a metal-semiconductor junction forms the metal wavefunction extends into the semiconductor energy gap. The tunneling of charge from the metallic overlayer into the semiconductor band gap induces continuum localized states at the initial interface in the semiconductor. As first discussed by Heine [8], the MIGS within the gap are Bloch states of the bulk semiconductor with complex wave vector and decay exponentially inside the semiconductor, but still have significant amplitude a few layers from the interface. The form of the MIGS in the semiconductor is determined by the volume band structure. Figure 5a illustrates a localized wavefunction tailing into both vacuum and the semiconductor band gap at a semiconductor surface. Figure 5b shows the metal wavefunction extending into the semiconductor energy gap when the junction forms. In turn, the new density of states associated with the metallic wavefunction tail can alter the densities of states in the conduction and valence

band, as shown in Fig. 5c for different separations *d* of the metal and semiconductor [60]. Here, an one-dimensional density of interface states develops around the semiconductor energy gap, associated with a resonance at mid-gap. In this model, the surface states, which are neutral when half-filled, define a charge neutrality level. Any deviation from

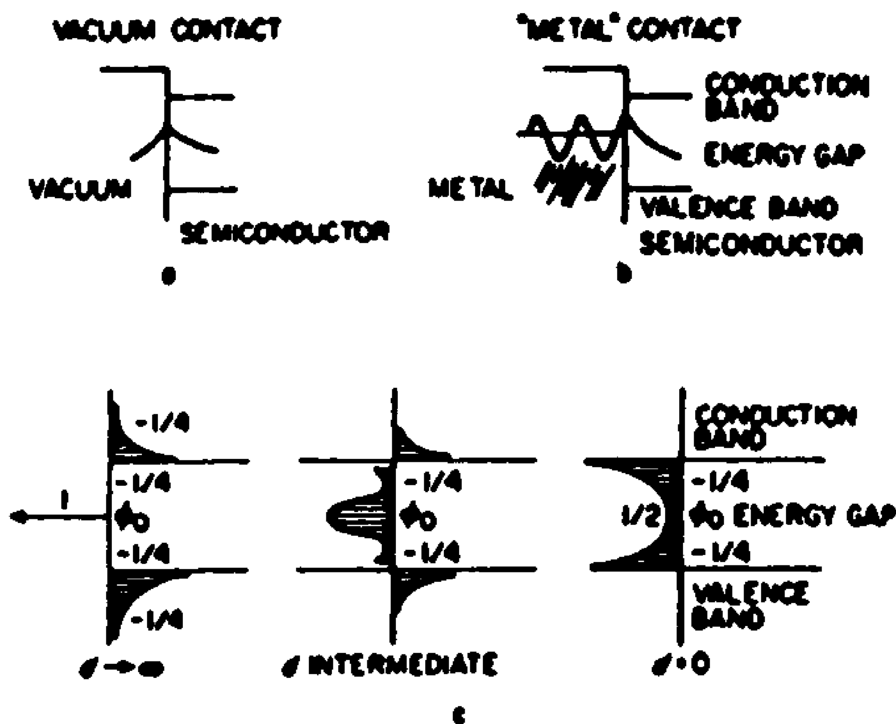

Figure 5. Localized wavefunction tunneling (a) into both vacuum and the semiconductor band gap at a semiconductor surface and (b) into the semiconductor band gap at a metal-semiconductor interface. The exponentially decaying behavior leads to a continuous density of intensity of interface states shown in (c) (after F. Flores and C. Tejedor, Ref. 60) for a one-dimensional model of a covalent semiconductor-metal interface.

local charge neutrality in the interface region results in "metallic" screening by the MIGS. Tersoff related such a charge neutrality level at mid-gap with the branch point of the complex band structure in a semiconductor [10].

A variation of this model involves a continuum of interface states due to atomic disorder, e.g., disorder-induced gap states (DIGS) [11]. Common features of such metal-induced gap states models are that (a) the density of states in the band gap exhibits a minimum at the point of Fermi level stabilization and (b) variations in barrier height are perturbations from the charge neutrality point whose magnitude scales with the dielectric response, i.e., high dielectric screening produces small deviations and vice versa. Thus ionic semiconductors with lower dielectric responses will permit larger deviations, as opposed to more covalent semiconductors such as GaAs and Si.

C. Advanced Unified Defect Model (or Antisite Defect Model) (ADM)

Defect models [3,12,48] of Fermi level pinning are based on the fact that only two relative constant Fermi level positions have been found by XPS for different 1 ML or less adsorbates on n- and p-type, UHV-cleaved GaAs (110) surfaces as shown in Fig. 6a. The ADM states that the perturbation of the semiconductor due to the deposition of metal produces native defect levels in the semiconductor just inside the interface and that these states are responsible for the Fermi

level pinning.

Figure 6a indicates a 0.2-0.3 eV gap between n-and p-type GaAs permitting significant overlap within an otherwise narrow energy range. Spicer *et al.* hypothesized that the two mid-gap energies in Fig. 6a are double donor levels related to an As

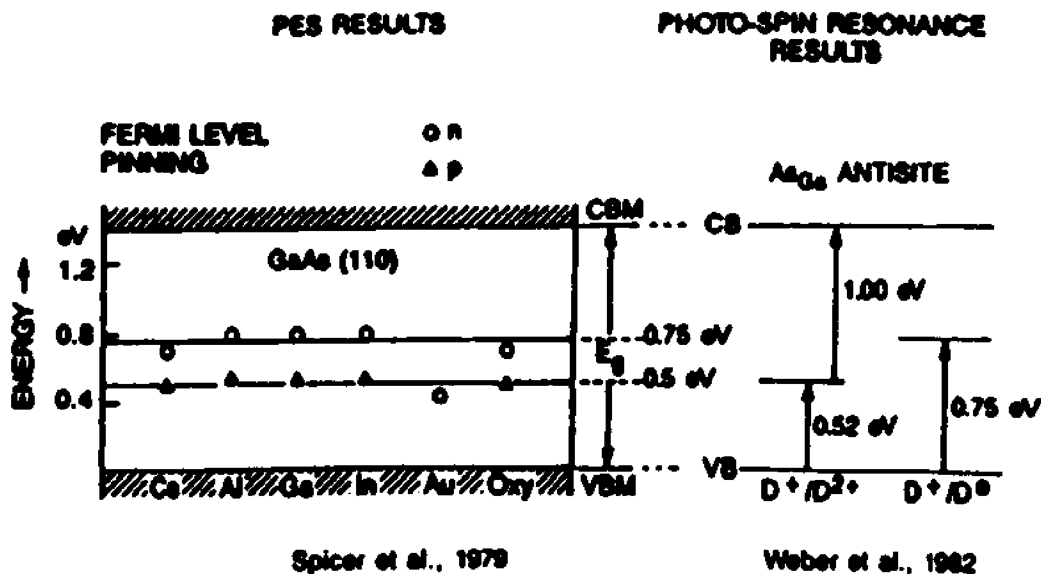

Figure 6. The diagram to the left is taken from Ref. 12. This energy level diagram indicates the pinning positions measured by XPS on n- and p-type GaAs (110) surfaces with very low coverages (order 1ML or less) of the indicated element at room temperature (E_g-1.42eV). The relatively constant energies for different adsorbates suggest that native defects (i.e., antisite defects) associated with the semiconductor rather than the adatom are responsible for pinning the Fermi level. The right diagram indicates the energy of the As_{Ga} antisite levels from the valence band maximum measured at 8K (E_g=1.52eV) by Weber et al. [61].

antisite defect complex [12]. Theoretical approach by Allen and Dow suggests the antisite defects have properties which makes it a strong candidate for being the dominant defects in the interfacial region [13]. The assignment of an As antisite defect related double donor levels is consistent with the energy level scheme deduced by Weber, as shown in Fig. 6b, for the As_{Ga} based on photo-electron paramagnetic resonance (EPR) spectra [61]. Depending on the electronegativity of the metal overlayer, the Fermi level will shift between the donor level energies. Furthermore, with changes in Ga-to-As stoichiometry produced by the metal-GaAs interface chemistry, the number of As antisite defects will increase or decrease, presumable raising or lowing the donor level occupancy (and thereby the Fermi level) in the band gap. A key aspect of this model is the observation that major changes in interface chemistry and cation/anion stoichiometry produce Fermi level changes which do affect pinning positions. However, it should be noted that the presence of excess As or Ga at the interfaces alone is insufficient to explain Fermi level shift in terms of antisite defects. As explained earlier, the EFW model can also predicts the Fermi level movement for different cation/anion stoichiometry. One must assume that the excess leads to an increase of As_{Ga} or Ga_{As} in the interface region of the GaAs crystal. In another words, excess As or Ga must be incorporated into the GaAs as antisite defects.

A quantitative calculation done by Zur, Mcgill, and

Smith [62] has shown that for Schottky barriers formed by thick metal contacts, there can be only one pinning position for both n- and p-type materials and that regardless of the mechanism, pinning will not occur for "surface defect" densities of less than about one monolayer. Also, as recently pointed out by Hecht [18] and confirm by several groups [4,19,20], surface photovoltage effects in XPS are important factor. It thus appears that the underlying assumption in previous photoemission work on band bending and Schottky barrier height determination needs experimental confirmation in each case. Therefore, it may be regarded as established that much of the previous data on low coverage and coverage-dependent Fermi level positions on III-V semiconductor surfaces, and in particular those at low doping and low temperature, needs to be re-examined.

D. Other Extrinsic Trap States

Other extrinsic Surface/interface States could arise due to chemical reactions, interdiffusion, new compound phases, as well as metal-induced states based on the localized metal/surface atom bonding [63]. Experimental results of the early 1970's provided early indications that chemical phenomena were playing a role in the interface electronic structure. Thus changes in barrier heights were observed with metal-semiconductor interdiffusion which were associated with the formation of electrically active sites. Measured barrier heights could be parametrized in terms of the thermodynamic

bond strengths and energies associated with a metal-semiconductor reaction. Analysis of semiconductor outdiffusion using XPS and AES revealed that the strength of localized bonding determined the anion /cation stoichiometry at the intimate junction and this stoichiometry correlated with a observed transition in barrier heights [64,65]. Recently the on intentionally misoriented (off axis) GaAs (100) surface has shown that major deviations from Schottky-like behavior can be produced via chemical interactions [15]. Step orientation rather than the presence of steps alone determines densities of chemically active sites at steps edges, which in turn results in order of magnitude changes in reaction and diffusion.

The electrical barriers associated with such semiconductor outdiffusion, metal indiffusion and compound formation may arise from the creation of new electrically active sites in the semiconductor and /or new dielectric layers at the interface. These electronic phenomena are associated with somewhat diverse models of Schottky barrier formation described in above sections.

CHAPTER II

MODULATION SPECTROSCOPY

2.1 Principle and Techniques of Modulation Spectroscopy

The basic idea of modulation spectroscopy is a very general principle of experimental physics [66-70]. Instead of directly measuring an optical spectrum, the derivative with respect to some parameter is measured. This can easily be accomplished by modulating some parameter of the sample, such as electric field, and measuring the corresponding normalized change in the optical properties. Structure in the conventional optical spectra, such as absorption spectra, is considerably enhanced in the derivative spectra and structureless backgrounds are eliminated. While it is difficult to calculate a full reflectance spectrum it is possible to account for the lineshape of localized spectral features of modulation spectroscopy.

Differential changes in the reflectivity can be related to the perturbation of the complex dielectric function ε expressed as [66,67]:

$$\Delta R/R = \alpha\Delta\varepsilon_1 + \beta\Delta\varepsilon_2 \qquad (4)$$

where R is the reflectivity, $\Delta\varepsilon_1$ and $\Delta\varepsilon_2$ are the changes in the complex dielectric function, $\varepsilon = \varepsilon_1 + i\varepsilon_2$. α and β are the Seraphin coefficients, which are related to the unperturbed dielectric function. $\Delta\varepsilon_1$ and $\Delta\varepsilon_2$ are related by a Kramers-Kronig inversion. The functional form of $\Delta\varepsilon_1$ and $\Delta\varepsilon_2$ can be calculated for a given perturbation provided that the dielectric function and type of critical point are known.

The modulation techniques can be classified into two categories: "external" and "internal" modulations [67-69]. In the external modulation a material is modified directly by applying a repetitive perturbation such as electric field (electromodulation), heat pulse (thermomodulation), or stress (piezomodulation). Changes in the measuring system itself, e.g., the polarization/wavelength of the probe light can be modulated or the sample reflectance can be compared to a reference sample (or portion of the sample), are termed internal modulation. The internal modulation is differential reflectomery and is simpler from the theoretical point of view since it involves only the optical properties of an unperturbed system. On the other hand, external method is simpler from the experimental point of view.

The external modulation can be subdivided into two groups according to the nature of the perturbation. Perturbations such as stress [71] or temperature [72] preserve the translational symmetry of the material. In this

situation for a transition the momentum conservation must be satisfied, i.e., $\Delta k = 0$ and either the energy gap or the broadening parameter or both have been modulated which usually gives rise to the first derivative-like spectra. Other perturbations like electric field [67] or magnetic field [66] destroy the translational invariance. In this case, forbidden transitions of $\Delta k \neq 0$ become allowed which gives rise to complicated lineshapes usually corresponding to higher order derivative-like spectra. Interpretation of these kinds of spectra involves rather formidable problem of the optical property calculations of the material in the presence of a perturbation.

Among all kinds of modulations, electromodulation is the most useful method since it yields the sharpest structure and is sensitive to surface/interface electric fields [66-70]. Electromodulation (EM) can be accomplished in several ways, including contact and contactless modes. Four common contact configurations, designated as electroreflectance (ER), can be divided into "longitudinal" and "transverse" categories [67,69]. The "longitudinal" method can be applied in the semiconductor-electrolyte, semiconductor-insulator-metal (MIS), Schottky barrier or p-i-n configurations. In the "transverse" mode two metal electrodes are evaporated on the surface of the sample and EM is produced by applying a modulated high voltage across the gap (~1mm). However, this technique can only be used on materials with resistivities

greater than 10^8 ohm-cm [67,69]

Contactless electromodulation can be performed using (a) photoreflectance (PR), (b) a new contactless approach which uses a capacitor-like arrangement [34] or (c) electron-beam electroreflectance (EBER) [73] In EBER the sample and electron gun must be placed in an ultra-high vacuum chamber. The method of PR is not only contactless but requires no special mounting of the sample. PR and CER can be used in any transparent medium under a variety of conditions. In the section of experimental techniques the PR and CER methods will be discussed.

2.2 Lineshape Consideration of Electromodulation

Electromodulation is the most complex form of modulation spectroscopy. Its perturbation can destroy the translational symmetry of the material and hence can accelerate unbound electrons and/or holes [67-70,74]. As will be discussed below this is exactly the aspect of EM that produces a sharp, third-derivative lineshape under certain field conditions.

However, for bound states such as excitons, impurities, quantum wells or the uncoupled states of multiple quantum wells the perturbing field does not accelerate electrons and/or holes. These types of particles do not have translational symmetry and are confined in space. In this situation the modulating field can alter the binding energy of the particle (Stark effect). The lineshape has a first-

derivative character [69,74]

Electromodulation can be classified into three categories, i.e., low-, intermediate- and high-field regime depending on the relative strengths of certain characteristic energies [67-70,75]. In the first range $|h\theta| \leq \Gamma$ where Γ is the broadening parameter and $h\theta$ is referred to as electro-optic energy and is given by:

$$(h\theta)^3 = e^2h^2F^2/2\mu \tag{5}$$

In Eq. (5) F is the field and μ is the reduced interband mass in the direction of the field. In the intermediate-field case $|h\theta| \geq \Gamma$ but $eFa_o << E_g$, where a_o is the lattice constant (or an appropriate periodic length in microstructures) and E_g is the band gap. In this situation the band structure is unchanged. In the high-field regime the electro-optic energy is again much greater than the broadening but the $eFa_o \sim E_g$ so that Stark shifts are produced.

2.2.1 Third Derivative Spectroscopy (Low-field regime)

For the unbound situation the case of low field modulation from flatband will be considered, i.e., no built-in dc field. Below a simple physical derivation of the effects of an electric field on the dielectric function will be presented [74]. A more rigorous and elegant treatment can

be found in literature [67]. The energy, $E(F)$, gained by a free particle in an electric field F can be written as:

$$E(F) = q^2F^2t^2/2\mu \tag{6}$$

where t is the time. If we consider an optical structure near a critical point with energy E_g, the dielectric function has the general form:

$$\varepsilon = \varepsilon(E-E_g, \Gamma) + B \tag{7}$$

where E is the photon energy, and B is the featureless background.

The change in the dielectric function, $\Delta\varepsilon$, induced by a modulating electric field F_{ac}, is given by:

$$\Delta\varepsilon = \varepsilon[E-E_g+E(F_{ac}), \Gamma] - \varepsilon[E-E_g, \Gamma] \tag{8}$$

where we have assumed that the electric field does not change Γ. If the field is sufficiently small so that $E(F_{ac})<<\Gamma$ (low field regime), Eq. (8) can be expanded in a Taylor's series to yield:

$$\Delta\varepsilon = E(F)[(\partial/\partial E)\varepsilon[E-E_g, \Gamma] \tag{9a}$$

$$= (q^2F_{ac}{}^2t^2/2\mu)[(\partial/\partial E)\varepsilon(E-E_g, \Gamma)] \tag{9b}$$

In quantum mechanics, the time t, is also an operator:

$$t = ih(\partial/\partial E) \tag{9c}$$

so that Eq. (9b) becomes:

$$\Delta\varepsilon = (q^2 F_{ac}{}^2 t^2/2\mu) \ [(\partial^3/\partial E^3)\varepsilon(E-E_g, \Gamma)] \tag{10a}$$

$$= (h\theta)^3 \ [(\partial^3/\partial E^3)\varepsilon(E-E_g, \Gamma)] \tag{10b}$$

where the electro-optic energy $h\theta$ is given by Eq. (5) with $F=F_{ac}$.

Equation (10b) has all the essential features of low field EM. The quantity $\Delta\varepsilon$ is proportional to $F_{ac}{}^2$ (modulating field), inversely proportional to μ and has a lineshape that is the third derivative of the unperturbed optical function [67]. Thus, in contrast to the first derivative modulation techniques, EM will give sharper structure. Note also that the condition $E(F_{ac})<<\Gamma$ is equivalent to $(h\theta)<<\Gamma$ if we take $\tau\Gamma=h$, where τ is a characteristic lifetime.

A more rigorous derivation of low field EM yields the expression [67]:

$$\Delta\varepsilon = [(h\theta)^3/12E^2] \ [(\partial^3/\partial E^3)E^2\varepsilon(E-E_g, \Gamma)] \tag{11}$$

If the form of ε is a Lorentzian Eqs. (4) and (11) take a particularly simple form [67]:

$$\Delta R/R = (h\theta)^3 \, \mathrm{Re}[Ae^{i\phi}(E-E_g+i\Gamma)^{-m}] \quad (12a)$$

$$= (h\theta)^3 \, L(E-E_g,\Gamma) \quad (12b)$$

where

$$L(E-E_g,\Gamma) = \mathrm{Re}[Ae^{i\phi}(E-E_g+i\Gamma)^{-m}] \quad (12c)$$

In Eqs. (12a) and (12c) A is the amplitude, ϕ is a phase angle which accounts for Eq. (4) and the influence of non-uniform electric fields [67,69,70]. The lineshape factor $L(E-E_g,\Gamma)$ is independent of the modulating field in the low-field regime.

The parameter m in the lineshape factor of Eq. (12c) depends on critical point type. For a three dimensional M_o critical point, such as the direct gap of GaAs, ε can be expressed as:

$$\varepsilon \sim (E-E_g+i\Gamma)^{1/2} \quad (13)$$

In this case m=2.5. For a two-dimensional critical point m=3

[67].

2.2.2 Franz-Keldysh Oscillations (Intermediate Field Regime)

In the event that the low-field criteria is not satisfied but that $eFa_o \ll E_g$ the dielectric function can exhibit Franz-Keldysh oscillations. We shall give a simple physical picture of this phenomenon and then present the results of more rigorous theories. In the following discussion it will first be assumed that there is no lineshape broadening involved, i.e., $\Gamma=0$.

The physical picture of Franz-Keldysh oscillations is photon-assisted indirect interband transitions in the real space. Under the influence of an electric field F in the z-direction the energy bands are tilted by an amount qFz. An electron attempting to tunnel from the valence band into the conduction band sees a triangular barrier. If during the tunneling process the electron interacts with a photon of energy E the effective width of the barrier to be transversed has been made smaller. The classical WKB approximation gives the same result as a more detailed treatment so that the former will be utilized. The probability of transmission T through the barrier is given by:

$$T = \exp\left(-2 \int k\,dz \right) \tag{14}$$

where the integral is between the classical turning points and

$$h\, k^2/2\mu = E_g - E - qFz \qquad (15)$$

The integral yields:

$$T = \exp\,[\, -(4/3)\eta^{3/2}\,] \qquad (16a)$$

where

$$\eta = (E_g - E)/h\theta \qquad (16b)$$

Equation (16a) contains most of the essential features of FKO. For $\eta>0$ ($E<E_g$) the transmission probability is exponential as a consequence of the photon-assisted tunneling. However, for $\eta<0$ ($E>E_g$) the transmission probability becomes an oscillatory function.

In a more rigorous treatment it can be shown that for a three-dimensional critical point the dielectric function in the presence of a field F can be written as [67,69]:

$$\varepsilon(E-E_g,\, F) = 1 + [C(h\theta)^{1/2}/E^2]\{G(\eta) + iF(\eta)\} + D[2(E_g)^{1/2} - (E_g+E)^{1/2}]/E^2 \qquad (17a)$$

where

$$G(\eta) = \pi[Ai'(\eta)Bi'(\eta) - \eta Ai(\eta)Bi(\eta)] + (\eta)^{1/2}H(\eta) \qquad (17b)$$

$$F(\eta) = \pi[Ai'^2(\eta) - \eta Ai^2(\eta)] - (-\eta)^{1/2}H(-\eta) \qquad (17c)$$

The quantities $G(\eta)$ and $F(\eta)$ are referred to as electro-optic functions while $Ai(\eta)$, $Ai'(\eta)$, $Bi(\eta)$ and $Bi'(\eta)$ are Airy functions and their derivatives and $H(\eta)$ is the unit step function [67,69,76]. The parameters C and D are related to matrix element effects and can be considered constants over the vicinity of the critical point.

Plotted by the solid line in Fig. 7a is $\varepsilon_2(E-E_g,F)$, the imaginary part of Eq. (17a). The dotted line is $\varepsilon_2(E-E_g,0)$. It can be seen that the field produces FKO that are superimposed on top of the $(E-E_g)^{1/2}$ dependence of $\varepsilon_2(E-E_g,0)$ for a 3-D homogeneous critical point (M_o). In Fig. 7b is plotted the expression for

$$\Delta\varepsilon_2(\eta) = \varepsilon_2(E-E_g,F) - \varepsilon_2(E-E_g,0) \qquad (18)$$

$$= [C(h\theta)^{1/2}/E^2]F(\eta)$$

The curve in Fig. 7b looks qualitatively similar to Eq. (16a), i.e., an exponential tail for $\eta>0$ and an oscillatory

function for $\eta<0$. From Eqs. (16) and (18) the position of the nth extrema in the FKO is given by:

$$n\pi = (4/3\pi)[(E_n-E_g)/h\theta]^{3/2} + \phi \qquad (19)$$

where E_n is the photon energy of the nth extrema and ϕ is an

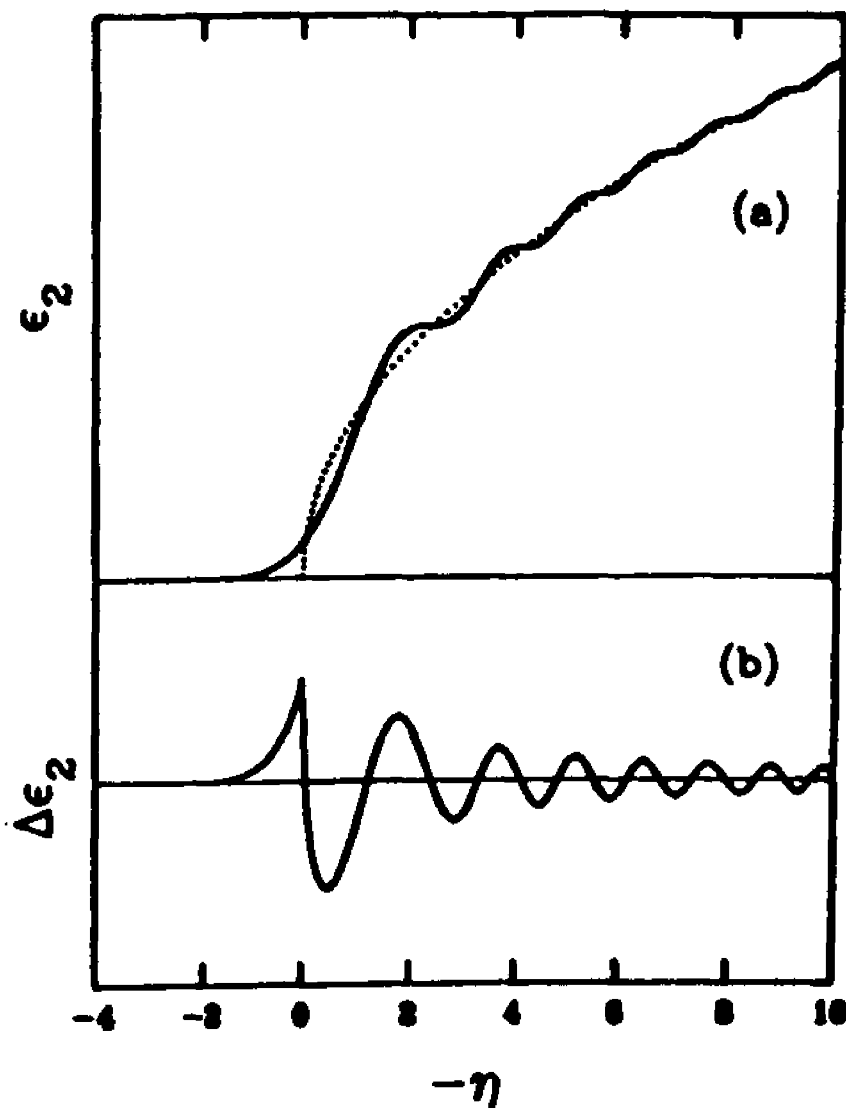

Figure 7. Plots of (a) $\epsilon_2(E-E_g,F)$ and $\epsilon_2(E-E_g,0)$ from Eq. (17) and (b) $\Delta\epsilon_2(\eta)$ from Eq. (18).

arbitrary phase angle [67,69,76]. A plot of $(4/3\pi)(E_n-E_g)^{3/2}$ versus index number n will yield a straight line with slope $(h\theta)^{-3/2}$. Therefore, the electric field, F, can be directly obtained from the period of FKO if μ is known. Or conversely μ can be measured if the field is known.

In the presence of Lorentzian broadening (Γ) the field-induced change in the dielectric function $\Delta\varepsilon(\eta,\Gamma)$ can be obtained from the unbroadened change $\Delta\varepsilon(\eta,0)$ using the expression [66,67,69,78]:

$$\Delta\varepsilon(\eta,\Gamma) = 1/\pi\int \Delta\varepsilon(\eta',0)\,\Gamma\, d\eta' / [(\eta-\eta')^2+\Gamma^2] \qquad (20a)$$

where Γ is in units of $h\theta$. A contour integration of Eq. (20a) yields:

$$\Delta\varepsilon(\eta,\Gamma) = \Delta\varepsilon(\eta + i\Gamma) \qquad (20b)$$

To illustrate the effects of broadening in Fig. 8 are plotted the values of the electro-optic functions $G(\eta,\Gamma)$ (solid) and $F(\eta,\Gamma)$ (dashed line) for Γ=1.0, 1.5 and 2.0 in units of $h\theta$ [78]. For the smallest Γ it is still possible to observe eight or nine FKO. The effects of

Γ becomes quite evident above about $-\eta=8$ in relation to the undamped case (see Fig. 7b). Only two or three FKO can still be seen for $\Gamma=1.5$ while $\Gamma=2.0$ the FKO are completely damped out. In this case the EM is in the third-derivative regime discussed in Sec. 2.2.1.

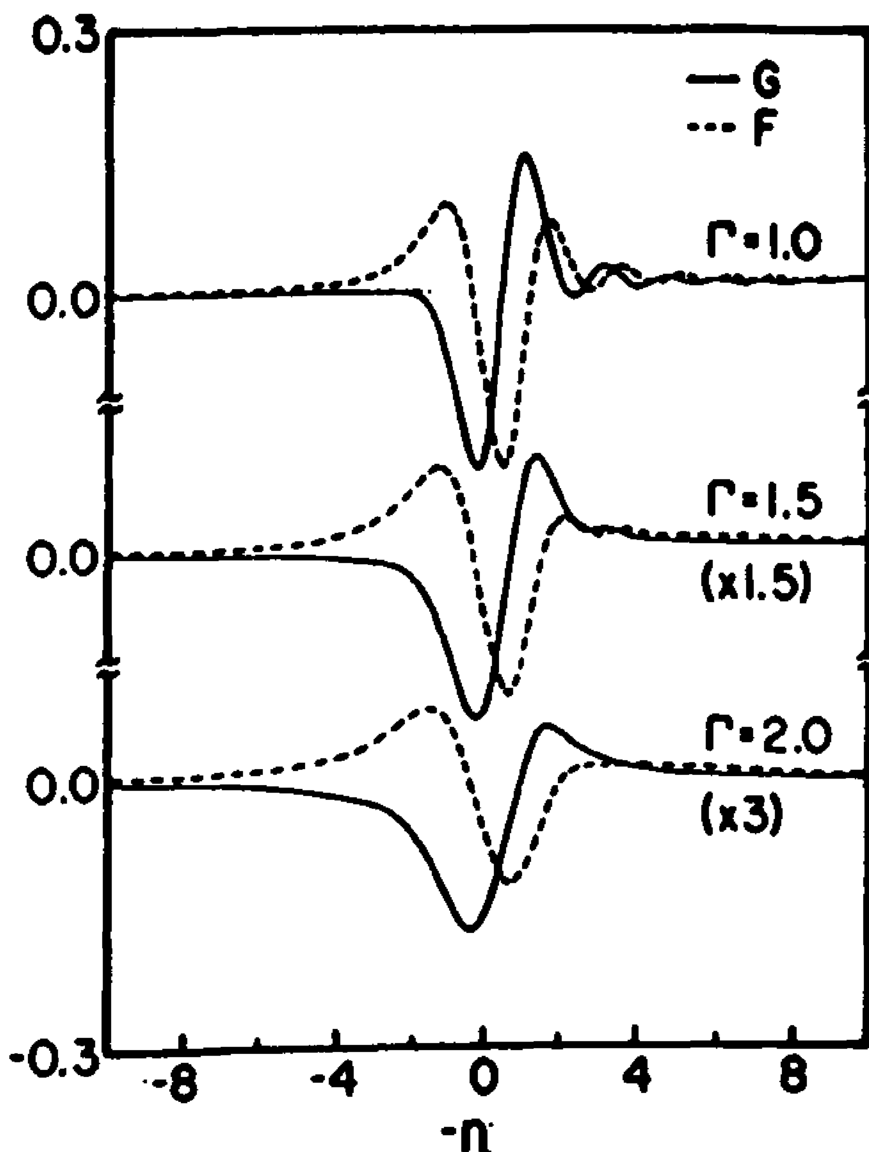

Figure 8. The electro-optic functions $G(\eta)$ and $F(\eta)$ for different values of the broadening parameter Γ (in units of $h\theta$) (after Shen and Pollak Ref.74).

Although the exact form of $\Delta R/R$ with broadening is fairly complicated a simple asymptotic expression can be written as [77,79]:

$$\Delta R/R \sim [E^2(E - E_g)]^{-1}\exp[-2(E - E_g)^{1/2}\Gamma/(h\theta)^{3/2}] \quad (21)$$
$$\times \cos\{(4/3\pi)[(E-E_g)/h\theta]^{3/2} + \phi\}$$

Aspnes [77] has stated that a plot of $\ln[E_n^2(E_n-E_g)]|\Delta R/R|_n]$ vs $2(E_n-E_g)^{1/2}/(h\theta)^{3/2}$ should yield a straight line with slope $-\Gamma$. However, care must be taken in utilizing this relationship to evaluate Γ since the densities of states of real materials may not remain parabolic sufficiently far from the critical point [69]. Also, for inhomogeneous fields the oscillations may not retain enough coherent to the degree needed. This may be the reason why Aspnes and Studna were not able to obtain accurate values of Γ by using Eq. (21)

The period of the FKO is determined by the dominant field in the structure. In the expression for $\varepsilon(E-E_g,F)$ [see Eq. (17)] the nature of that field was not specified. There are two limiting cases to be considered. If modulation is from flatband, i.e., no dc field then the field is clearly the modulating field, F_{ac}. Until recently most FKO studies were performed in this regime [67]. However, a more interesting situation occurs when there exists a large dc

electric field, F_{dc}, in the material and a small modulating field is applied, i.e., $F_{ac} << F_{dc}$. In this case the period of the FKO are given by F_{dc} and not F_{ac} [78].

The treatment of FKO discussed above has assumed a uniformed electric field. In the presence of non-fields, such as in the space-charge region (SCR) of a doped semiconductor semiconductor, the effective change in dielectric function $\Delta\varepsilon$ can be expressed as [67,69,78]:

$$\langle\Delta\varepsilon\rangle = -2i\kappa\int_0^\infty \exp(i2\kappa z')\Delta\varepsilon[E-E_g,F(z')]dz' \qquad (22)$$

where $\kappa(E)$ is the complex propagation vector of the light in the solid.

Several works have considered the effect of non-uniform fields on $\Delta\varepsilon$ in the FKO regime [21,22,31,78]. It has been clearly demonstrated that for small modulation the FKO are a measure of the maximum field in the structure not the average field [22,31]. For EM in small modulation situation not only is ε modulated but also the width (W) of the SCR. The resultant signal of Eq. (22) comes only from a small near-surface region $\Delta W(<<W)$, where ΔW is the change in the SCR induced by $F_{ac}(<<F_{dc})$. In this small portion of the SCR, the field is almost uniformed and equal to the surface (maximum)

field.

2.2.3 First-Derivative Spectroscopy

As discussed above the third-derivative nature of EM in the low-field regime is a consequence of the fact that the electric field can destroy the translational symmetry of the material and accelerate the electrons and/or holes. This is not true for bound states.

Confined system, such as the isolated states of quantum wells and multiple quantum wells, excitons, impurities, etc., differ significantly from the unbound states of bulk material because the particle (electron or hole) and its wave function are localized in space. Because of this confinement, the energies (in the confinement direction for microstructures) are discrete and dispersionless resulting in an infinite effective mass (in the confinement direction). An applied electric field (along the confinement direction) adds a linear potential, which tilts the confining potential, changing its shape. The electrons and holes become spatially polarized, but still remain confined. This alters both the electronic energies and the wave function overlap [intensity (I)]. Also the tilting of the potential can result in a change in lifetime Γ as a result of tunneling.

In terms of EM, the infinite mass means that Eq. (10b) and (18) are no longer applicable since $h\theta=0$. Several authors have treated this problem in detail. They have shown that

under these conditions the change in the dielectric function induced by the modulating field, F_{ac}, is first-derivative and can be expressed as [78,80-87]:

$$\Delta\varepsilon = [(\partial\varepsilon/\partial E_g)(\partial E_g/\partial F_{ac}) + (\partial\varepsilon/\partial\Gamma)(\partial\Gamma/\partial F_{ac}) + (\partial\varepsilon/\partial I)(\partial I/\partial F_{ac})]F_{ac} \qquad (23)$$

This equation can be rewritten as [88]:

$$\Delta\varepsilon_i = [A_E f_E^{(i)} + A_\Gamma f_\Gamma^{(i)} + A_I f_I^{(i)}](I/\Gamma)F_{ac} \qquad (24a)$$

with

$$A_E = (1/\Gamma)(\partial E_g/\partial F_{ac}) \qquad (24b)$$

$$A_\Gamma = (1/\Gamma)(\partial\Gamma/\partial F_{ac}) \qquad (24c)$$

$$A_I = (1/\Gamma)(\partial I/\partial F_{ac}) \qquad (24d)$$

and

$$f_E^{(i)} = (\partial\varepsilon_i/\partial E_g) \qquad (24e)$$

$$f_\Gamma^{(i)} = (\partial\varepsilon_i/\partial\Gamma) \qquad (24f)$$

$$f_I^{(i)} = (\partial\varepsilon_i/\partial I) \qquad (24g)$$

In the situations discussed above (excitons, impurities,

isolated quantum states) the unperturbed dielectric function of Eqs. (23) or (24) will be either Lorentzian or Gaussian, depending on the broadening mechanism and/or temperature [78,80-82,89]. For quantum wells the dielectric function is excitonic, even to elevated temperatures, because of the enhanced exciton binding energy caused by the reduced dimensionality. Thus the Lorentzian or Gaussian profile will be appropriate for these quantum microstructures.

It should be noted that in high quality bulk material grown by techniques such as MBE or VPE direct gap excitons may be present even at 300K [62]. In such cases the first-derivative lineshape form of Eq. (23) will be appropriate rather than the third-derivative profile for band-to-band transitions.

2.3 UN^{+} (UP^{+}) Structures

As mentioned in above section FKO can , in principle, be used as an effective way to evaluate surface/interface electric fields. However, in practice this has proven to be somewhat more difficult. For example, the electric field in the space-charge region of a bulk/thin film semiconductor is related to the donor (acceptor) concentration. In order to obtain fields high enough to observe FKO a certain doping level must be used. However, if the doping level becomes too high then, due to the impurity scattering, the damping parameter Γ of Eqs.(20) and (21) becomes so large that the

FKO are washed out and one gets the third derivative spectra. Thus FKO can only be observed in a narrow range of impurity concentrations of about 10^{15} - $10^{16}cm^{-3}$. Even for these samples only 4 or 5 FKOs are generally seen [23,69].

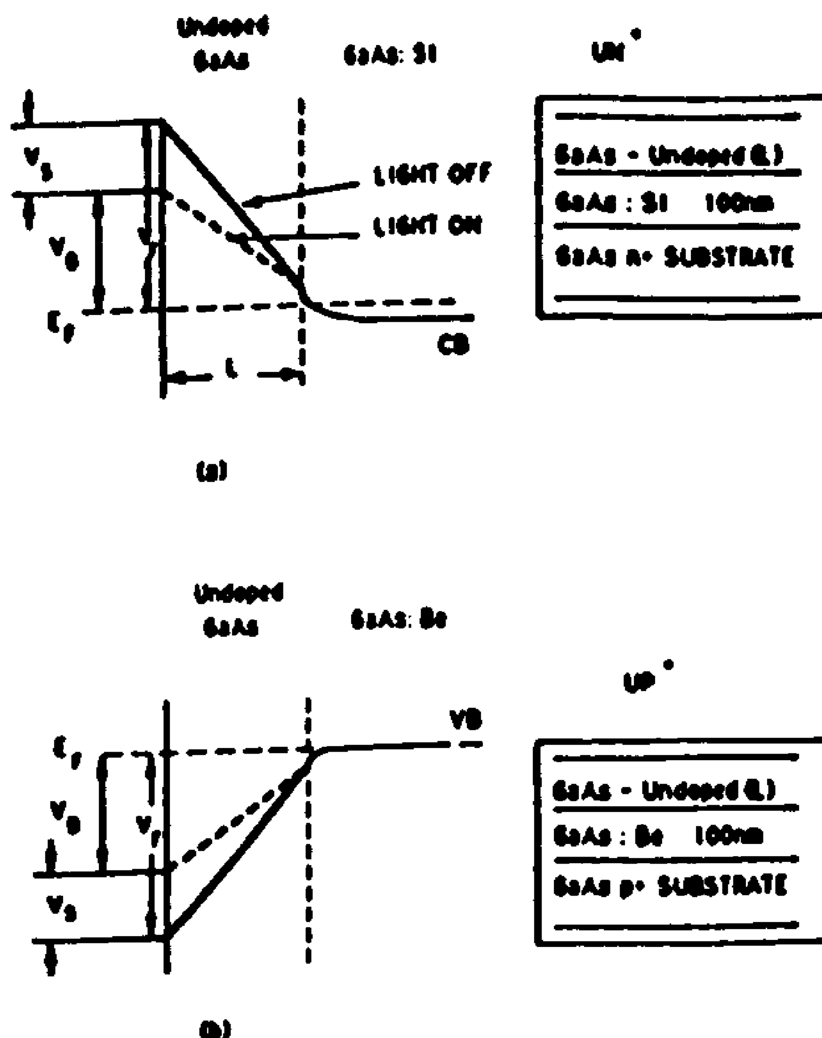

Firgure 9. Schematic representation of the band structures of (a) UN^+ and (b) UP^+ configurations for buffer doping levels of 2 x $10^{18}cm^{-3}$ for the UN^+ sample and 1 x $10^{18}cm^{-3}$ for the UP^+ sample. The influence of light on the barrier height is shown.

The above problem can be overcome by the use of

UN^+ (UP^+) structures [24-27,36] which are made by fabricating an undoped layer of thickness L (~1000A) on a buried n^+ (p^+) buffer (n or p~$1x10^{18}cm^{-3}$) on an n^+ (p^+) substrate. Such configurations, which are shown in Fig.9, have been designated UN^+ and UP^+ [25,28,29], respectively (or SIN^+ and SIP^+ in Refs. 24, 25).

In the buried n^+ (p^+) buffer/substrate the Fermi level occurs near the conduction (valence) band edge. At the surface the Fermi level is pinned at some value. Therefore, there exists in the undoped region, which has a small Γ, a large, almost constant electric field, F. Thus, these structures will exhibit a large number of FKO in PR spectrum. The field F, as directly measured by the FKO, can easily related to surface Fermi level pinning effects as discussed below.

Using the UN^+ (UP^+) structure samples from the FKO of their PR spectrum the electric field F can be accurately determined. A typical PR spectrum at 300K from a (001) GaAs UN^+ structure (L=110nm) is shown in Fig. 10 [25]. Note the large number of FKO. Plotted in the inset is $(4/3\pi)(E_n-E_g)^{3/2}$ versus index number n. The solid line is a least-squares fit to a linear function which makes it possible to accurately evaluate the electric field [see Eq. (19)], and hence the

built-in potential.

The relation between F and the barrier height, V_B, can be written as:

$$V_B = FL + (kT/q) + SCC. \qquad (25a)$$

where the second term is the Debye length correction and SCC is the space-charge correction of the buffer. For non-degenerate semiconductor the SCC is given by:

$$SCC = \varepsilon F^2/2qn^+(p^+) \qquad (25b)$$

where ε is the static dielectric constant of GaAs (=13.2) and n^+ (p^+) is the doping level in the buffer. Equation (25b) is a good approximation for the UP^+ sample ($p^+ \sim 1 \times 10^{18}$ cm^{-3}) since the Fermi level in the buffer is close to the valence band edge (VB). However, for the UN^+ material ($n^+ \sim 2 \times 10^{18} cm^{-3}$) the doping level is such that the Fermi level occurs about 0.075 V above the conduction band edge (CB). In this degenerate situation the SCC must be written as:

$$SCC = (4/3\pi)(kT/q)(N_C/n^+)[F_{3/2}(-\varepsilon F^2/2qn^+) - F_{3/2}(0)] \qquad (25c)$$
$$+ \varepsilon F^2/2qn^+$$

where N_c is the density of states in the conduction band and $F_{3/2}(x)$ is the Fermi integral of argument x.

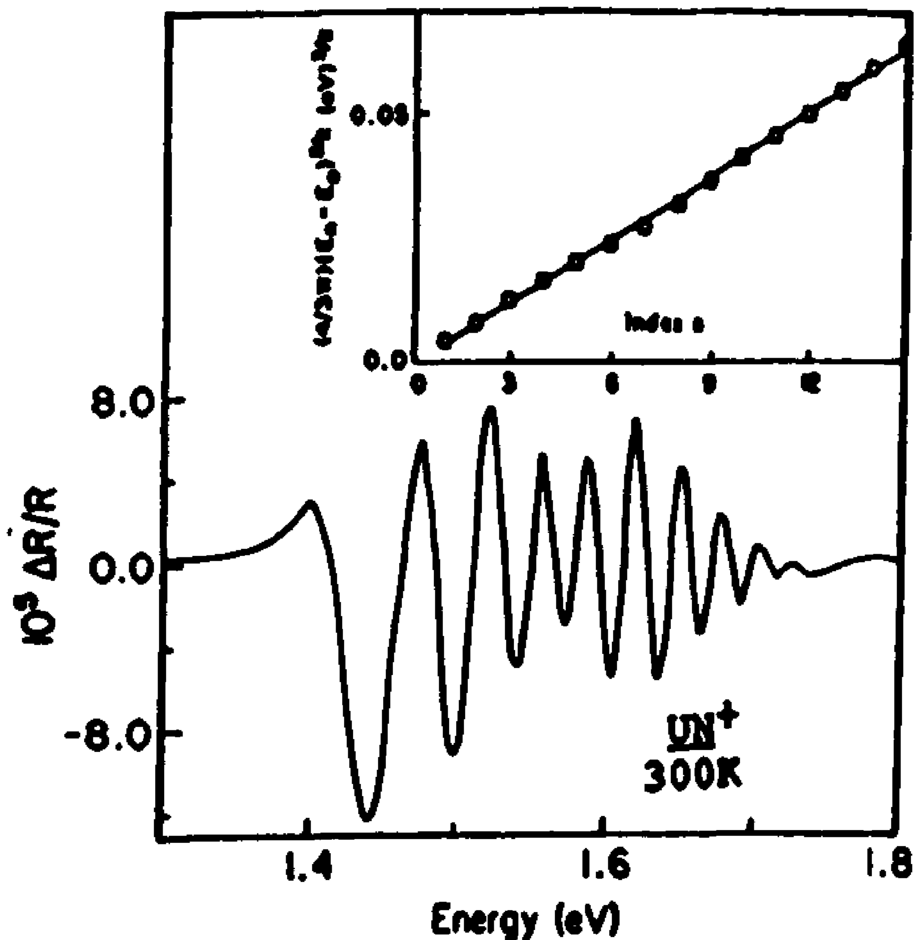

Figure 10. Photoreflectance spectrum of the UN^+ sample at room temperature with P_{pu} = 3μW-cm^{-2} (633nm line) and P_{pr} = 2μW-cm^{-2}. The inset shows a plot of $(4/3\pi)(E_n-E_o)^{3/2}$ as a function of FKO index n.

The effect of light on V_B is also shown schematically in Fig. 9. The measured barrier height V_B is equal to the Fermi

level position (V_F) minus the surface photovoltage (V_S) induced by the pump/probe light, i.e., $V_B = V_F - V_S$. Thus, if V_S can be eliminated or determined V_F can be accurately obtained. The detailed discussion will be given in the following chapter.

2.4 Experimental Techniques

2.4.1 Photoreflectance

In PR modulation of the electric field in the sample is caused by photo-excited electron-hole pairs created by the pump source (laser or other monochromatic light source) which is chopped at frequency Ω_m. The photon energy of the pump source must be above the bandgap of the semiconductor being investigated. A typical pump source is a 5mW He-Ne laser. The photo-excited free carriers can perturb the reflectivity by various mechanism including: a) screening of excitons, b) Burstein-Moss effect (band filling effect), c) reduction of the built-in electric field through the recombination of minority carriers with the majority carrier in surface/interface region. In PR, with a typical low light intensity pump source ($\leq$ 100mW/cm^2), mechanism (c) is dominant [67,69].

Shown in Fig. 11 is a schematic representation of the PR apparatus. Light from an appropriate lamp source passes through a monochromator (probe monochromater). The exit

intensity at wavelength λ, $I_o(\lambda)$, is focussed onto the sample by means of a lens (or mirror). The reflected beam is collected by a second lens (mirror) and is focussed onto an appropriate detector. For the sake of simplicity we have not shown the two lenses (mirrors).

The light striking the detector contains two signals: a) the dc (or average value) is given by $I_o(\lambda)R(\lambda)$, where $R(\lambda)$ is the dc reference of the material, b) the modulating value (at frequency Ω_m) is $I_o(\lambda)\Delta R(\lambda)$, where $\Delta R(\lambda)$ is the modulated reflectance. The ac signal from the detector, proportional to $I_o\Delta R$, is measured by a lock-in amplifier (LIA). In order to evaluate the quantity of interest, i.e. the relative change in reflectance $\Delta R/R$, a normalization procedure must be used to eliminate the uninteresting common factor $I_o(\lambda)$. In Fig. 11 this normalization is performed by the variable neutral density filter (VNDF) connected to a servo mechanism. The dc signal from the detector, which is proportional to $I_o(\lambda)R(\lambda)$, is introduced into the servo which moves the VNDF in such manner as to keep $I_o(\lambda)R(\lambda)$ as a constant, i.e., $I_o(\lambda)R(\lambda)=C$. Under these conditions the ac signal $I_o(\lambda)\Delta R(\lambda)=C\Delta R(\lambda)/R(\lambda)$. Thus, the signal to the LIA is proportional to the quantity of interest, i.e., $\Delta R(\lambda)/R(\lambda)$.

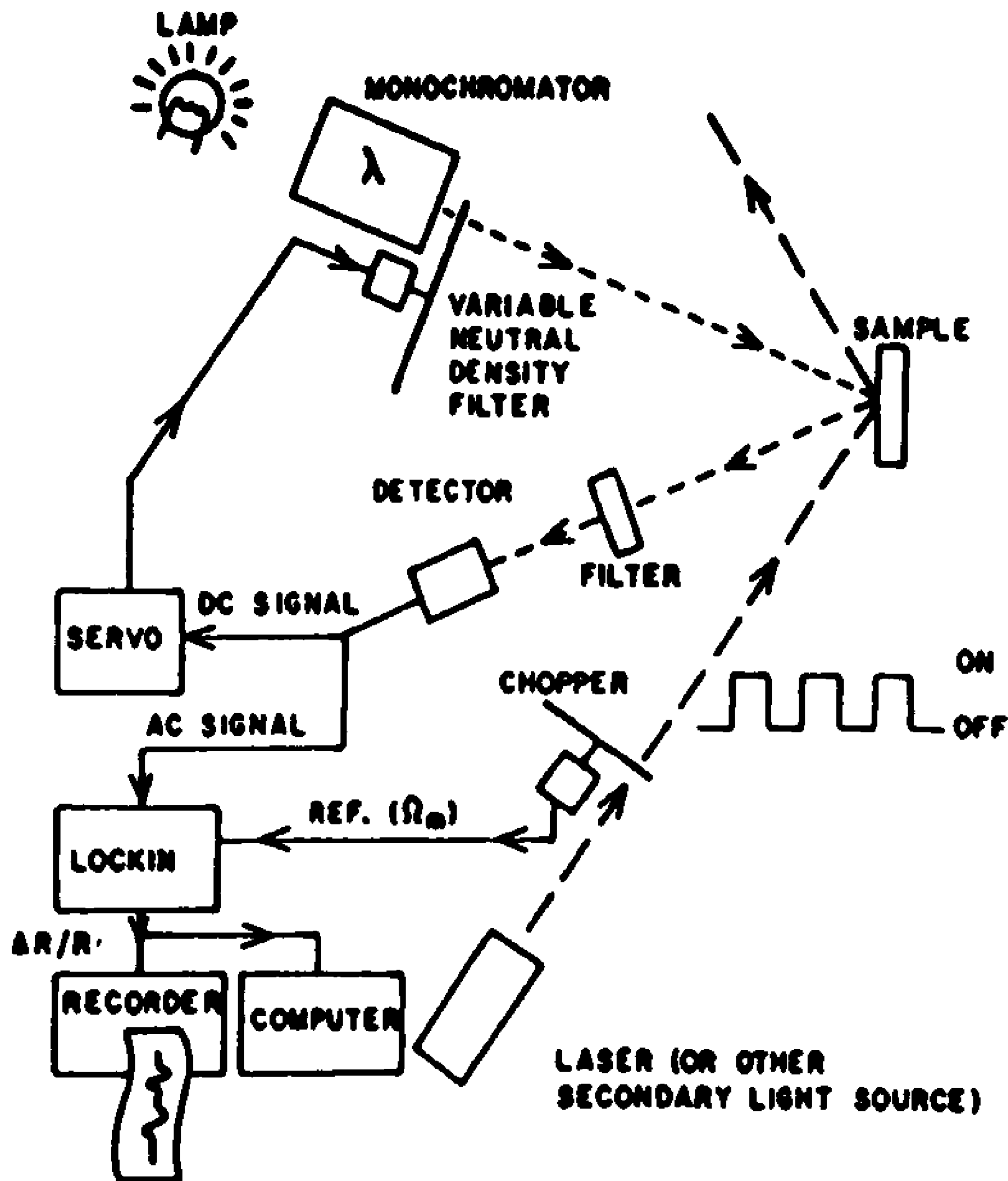

Figure 11. Schematic function block diagram of photoreflectance set up.

It should be point out that since PR is a normalized optical method not every photon need to be collected. For

example, if there is some obstruction on a viewport so that a fraction of the light is lost then the light striking the sample is only αI_0, where $\alpha < 1$. Thus the dc reflected component will be $\alpha I_0 R$ and the ac signal is $\alpha I_0 \Delta R$. However, the normalized signal is still proportional to $\Delta R/R$. Therefore as long as there are enough photons to give a good signal-to-noise ratio the lineshape of the PR signal is not affected by the loss of some light.

The entire apparatus is under computer control. The computer drives the probe monochromator and the normalization mechanism. The computer is also used for data analysis such as FKO and lineshape fits.

A drawback of PR is the spurious modulated background signal reaching the detector because of (a) luminescence from the sample and/or (b) scattered light from the pump source. Luminescence can sometimes be a problem for measurements near the fundamental gap, particularly at low temperature. Scattered pump light can be reduced by means of an appropriate long pass filter in front of detector. If the overall spurious background signal is not too large in relation to $\Delta R/R$ it can be subtracted by the normalization method Fig. 11.

The spurious signal also can be reduced or eliminated by approaches such as the use of a double monochromater [91], tunable dye laser probe beam [92], sweeping PR [93] or

differential PR [94].

2.4.2 New Contactless Mode of Electromodulation

Shown in Fig. 12 is a schematic block diagram of a contactless electroreflectance (CER) system. In contrast to PR method, in CER the modulating field is directly applied to the sample by an ac power supply (~ 1kV peak-to-peak) with an option of dc bias. The CER method utilizes a condenser-like system consisting of a thin, transparent, conductive coating (indium-tin-oxide or 5-6nm of a metal such as Au or Ni) on a transparent substrates (glass, quartz, etc.) which serves as one electrode [34]. A second electrode consisting of a metal stripe is separated from the first electrode by insulating spacers. Figure 13 is a schematic view of the condenser-like arrangement used in the CER. The sample (~0.5mm thick) is placed between the two capacitor plates. The dimensions of the spacer are such that there is a very thin layer (~0.1mm) of air (or vacuum) between the front surface of the sample and the conducting part of the first electrode. This can be accomplished by (a) varying the thickness of the insulating spacers or (b) mounting the first/second electrode on a micrometer. Thus, there is nothing in direct contact with the front surface of the sample. The ac modulating (~1kV peak-to-peak) and dc bias voltages are applied between the metal strip and the transparent conductor. The probe beam is incident through the first transparent electrode. This approach can also be employed in the transmission mode by

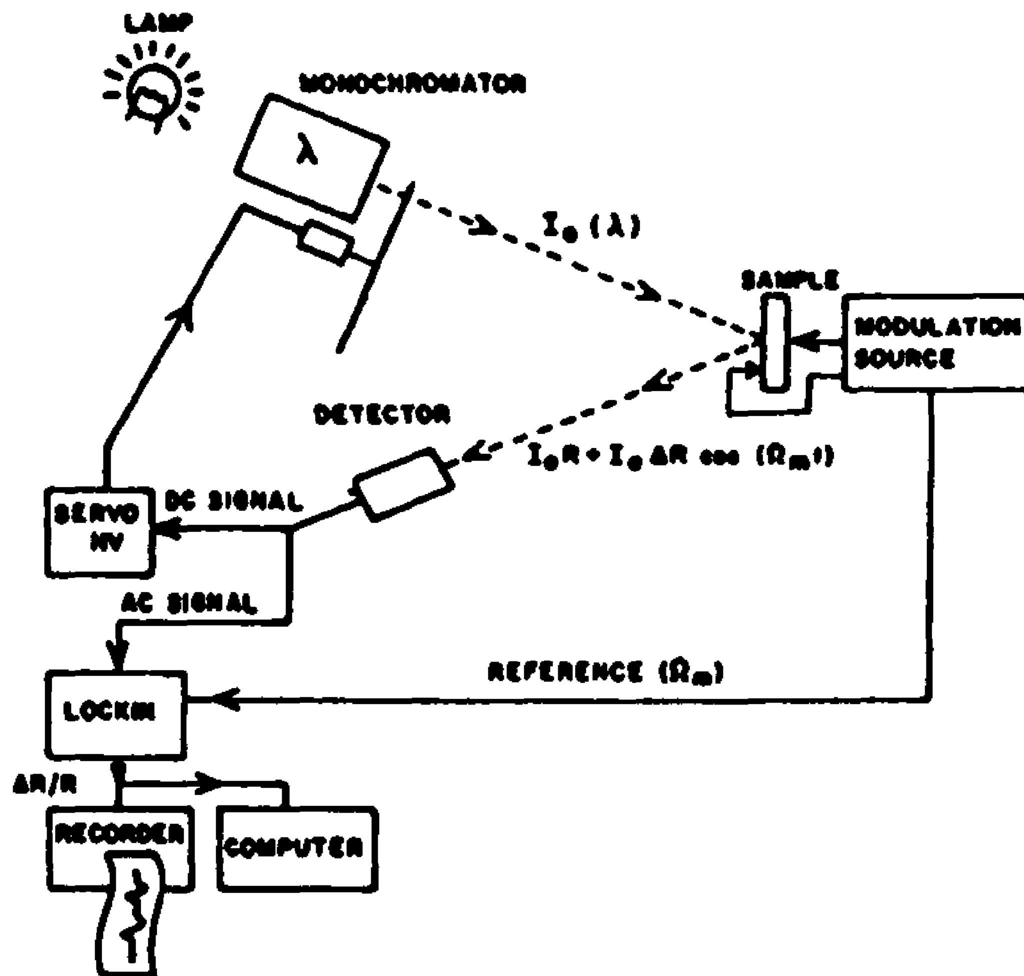

Figure 12. Schematic function block diagram of CER set up.

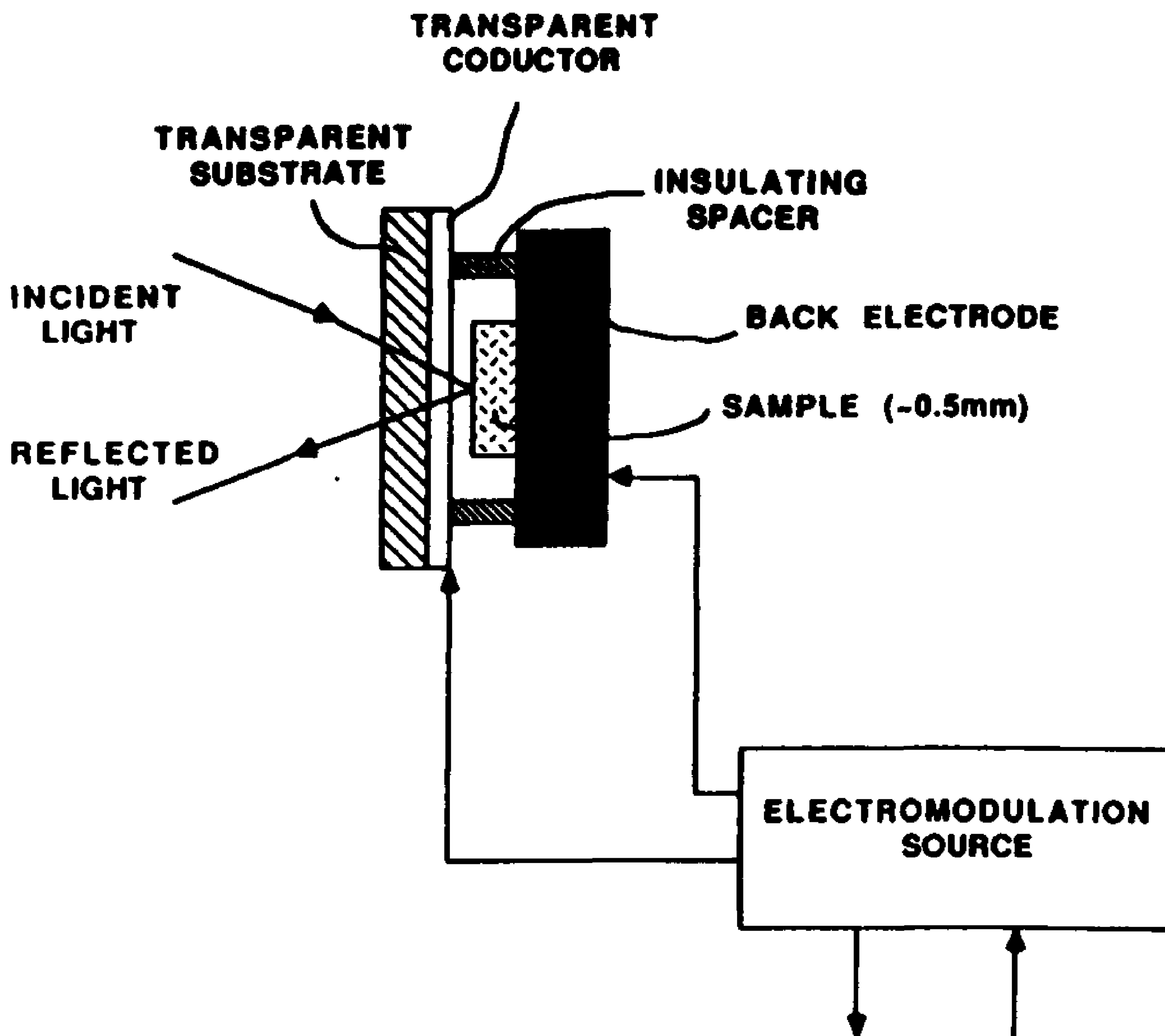

Figure 13. Schematic view of the condenser-like arrangement used in CER system (see Fig. 12).

replacing the metal electrode with a second transparent electrode/substrate.

Shown by the solid lines in Fig. 14 are the CER and PR spectra at 300K of a sample of polished (001) semi-insulating (SI) bulk GaAs (~0.5mm thick) grown by the liquid

encapsulated Czrochralski method. The PR data was taken using

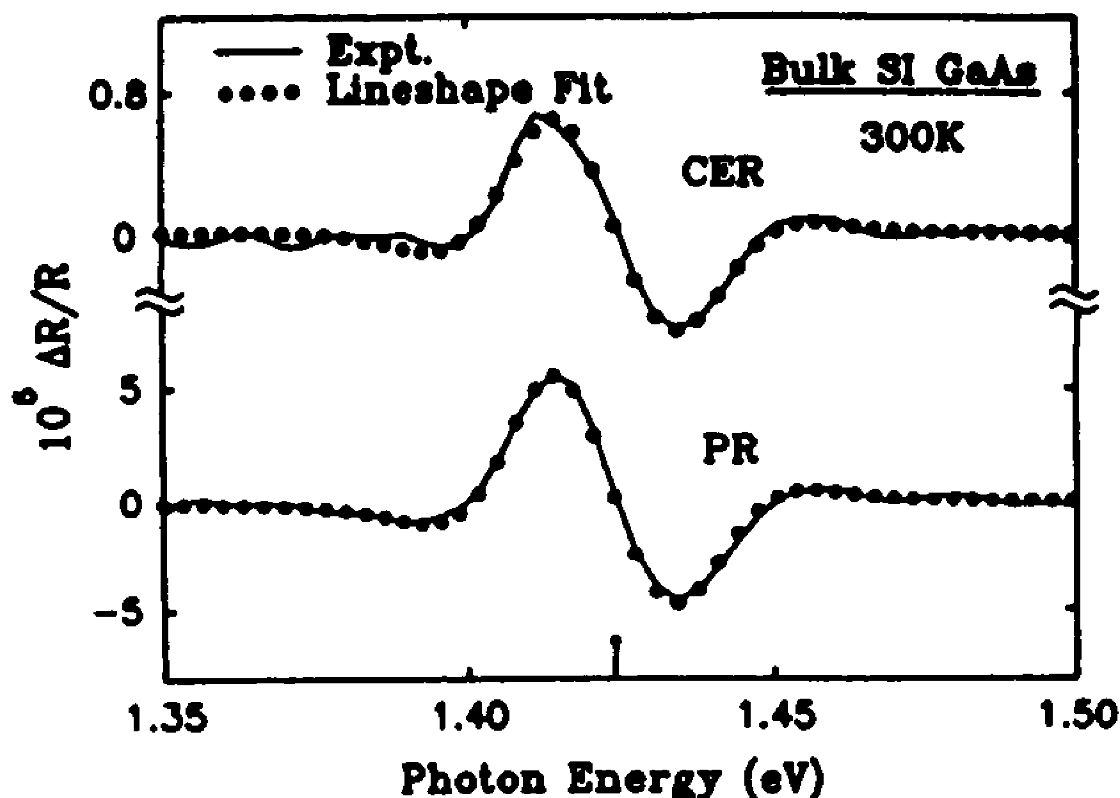

Figure 14. The CER and PR spectra of bulk semi-insulating GaAs at 300K. The dotted lines are a least-squares fits for a FDGL.

a 3mW He-Ne chopped at 200Hz as the pump source [95]. The CER measurements were obtained using a modulating voltage of 500V (peak-to-peak) at 200Hz. The spectra are in the range of the fundamental band gap (E_0) of GaAs. We find that the best fit to the data is obtained using a first-derivative Gaussian

lineshape (FDGL) function [74] (dotted lines) rather than the Aspnes third-derivative functional form [67] (TDFF) lineshape. The FDGL is appropriate for an exciton [74] associated with E_o at 300K. The obtained energy of 1.424 eV for E_o for both CER and PR is designated by the arrow at the bottom of the figure. Note that the two spectra are almost identical. Since PR produces EM this comparison demonstrates that CER also is an EM method.

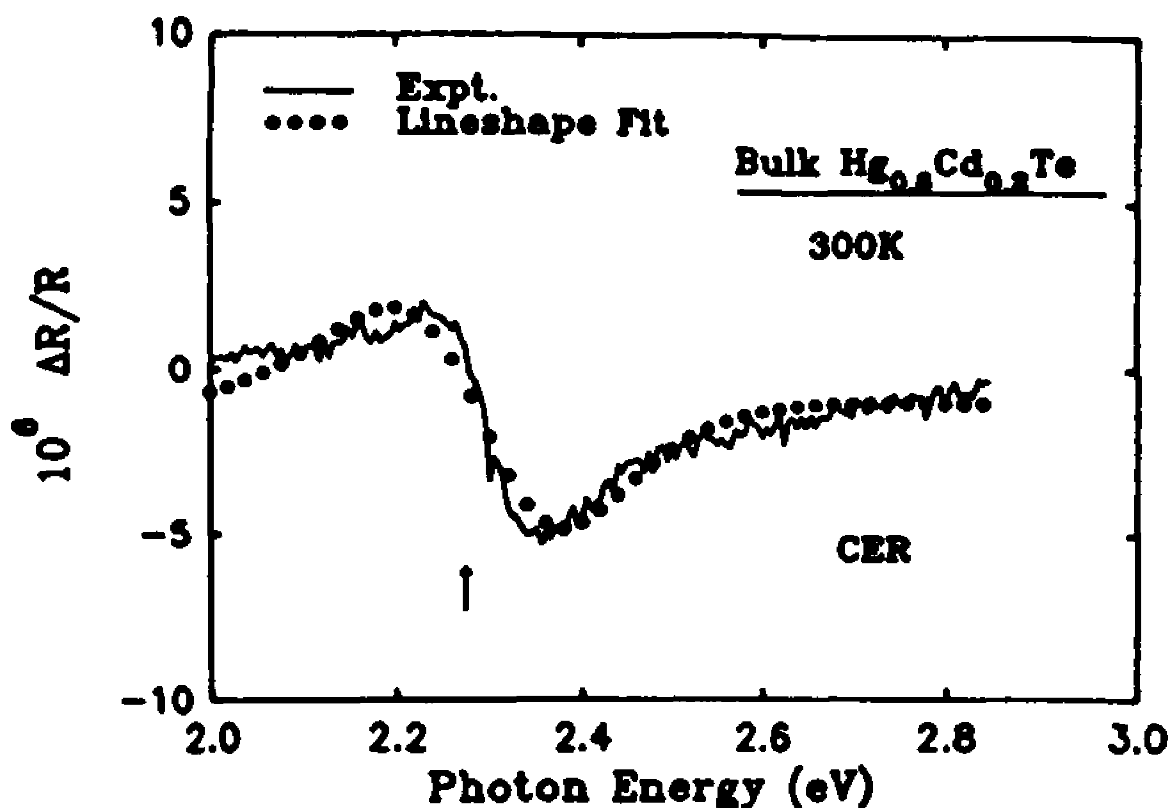

Figure 15. The CER spectrum of bulk $Hg_{0.8}Cd_{0.2}Te$ at 300K. The dotted line is a least-squares fit to a TDFF for a two-dimensional critical point.

The CER spectrum of a bulk $Hg_{0.8}Cd_{0.2}Te$ sample at 300K in the range of the E1 feature is displayed in Fig. 15. No PR signal at 300K could be obtained from this narrow gap sample. The solid line is a least-squares fit to a TDFF for a two-dimensional critical point [67-69,74]. The obtained energy enables us to determine the Hg composition [68]. These results are extremely significant since in the past it has not been possible to obtain signals from narrow gap $Hg_xCd_{1-x}Te$ (x=0.2-0.3) at 300K using other contactless EM methods such as PR or EBER [73]. These experimental techniques have yielded signals only at 77K or below [96].

Our newly developed CER method has a number of advantages over PR. Since there is no chopped pump beam in CER there is no photoluminescence background as often occurs in the PR signal of high quality samples, particularly at low temperatures [68,69]. Also in order to obtain a PR signal there must be a built-in field. The field drives photo-excited minority carriers to surface/interface charge traps creating the EM. While in CER the EM is produced by simply applying an ac voltage (with a dc bias if necessary).

In addition, from the phase of the CER signal the nature of the band bending (carrier type) at the surface of a semiconductor with a built-in electric field can be evaluated. Our results on various semiconductors will be presented in Chapter three. EBER [73] can be also used for this purpose. However, the phase of the minority carrier PR method does not apply.

CHAPTER III

EXPERIMENTAL RESULTS

Almost since its inception it has been recognized that EM could be used as an effective probe of surfaces and interfaces. This is not only because of the sharp, derivative-like features but also because of its sensitivity to electric fields. In addition to spectral features other variables such as phase and pump wavelength (in the case of PR) can provide important information. However, until recently little work has been done in this area. For example, as discussed earlier the FKO observed in EM are a direct measure of the built-in dc electric field that exists at surface/interface due to Fermi level pinning. The nature of the surface band bending, including flat band, can be determined by the phase of EM methods such as ER, CER and EBER. Furthermore, the contactless forms of EM such as PR and CER employ very low light levels, require no special mounting of the sample (in the case of PR), and can be performed in any transparent ambient including ultra high vacuum [25,26,31,32]. Thus contactless EM methods provide a versatile tool which can accurately measure V_F in a variety of ambients and semiconductor interfaces e.g. vacuum, air, metal/semiconductor, or semiconductor/semiconductor interfaces, etc.

In this chapter we will first present a photoreflectance study of Fermi level pinning (V_F) on the (001) UN^+ and UP^+ GaAs structures. Surface photovoltage (V_S) effects were evaluated as a function of temperature (77K < T < 450K), pump beam wavelength (633nm and 407nm) W-metal coverage (in-situ) and light intensities (probe, pump and dc light). The dependence of the measured barrier height, V_B (= V_F-V_S), on T can be explained by a modification of the theory of M. Hecht [18]. In addition, by introducing the ratio (r) of the area of the surface states to the illuminated area into the theory of Hecht we have been able to estimate the density of surface states on the GaAs surface.

Studies of the surface barrier height on (001) MBE grown GaAs under a variety of conditions including air, ultrahigh-vacuum (UHV), sputter/annealing (in UHV), etc., will be presented. In addition, the surface/interface Fermi level pinning effects have been investigated on (001) MBE grown low substrate growth temperature As-rich GaAs(GaAs:As) using PR as well as CER. The implication of our results for various models of Schottky barrier formation will be discussed. The need to simultaneously measure both n- and p-type material in order to obtain unambiguous results will be demonstrated.

Our recent results on the nature of band bending at semiconductor surface characterized by CER also will be presented.

3.1 Surface Photovoltage Effects

The structures used in this study were prepared by molecular beam epitaxy (MBE) by fabricating an undoped layer of thickness L (= 110nm) on a buried 1μm Si-doped buffer (n^+ ~ $2x10^{18}cm^{-3}$) on an n^+ substrate and an undoped layer of L (= 220nm) on a 1μm Be-doped buffer (p^+ ~ $1x10^{18}cm^{-3}$) and a p^+ substrate. Such configurations have been designated UN^+ and UP^+ in Chapter II. The thickness L was evaluated from C-V measurements.

The PR measurements were performed separately with two different pump wavelength beams. They were the 633nm line of a 5mW He-Ne laser and the 407nm line of a Kr-ion laser both chopped at 100Hz. The values of pump beam (P_{pu}) and probe beam (P_{pr}) light intensities were controlled by neutral density filters and measured by a power meter. The study of the W-metal coverage was performed in-situ in a UHV chamber with an operating pressure of better than 1.5×10^{-10} Torr.

We have performed the PR measurements with different sizes of the illumination area for bare surface samples. They show no difference. This result implies that the surface current is not a important factor for these bare surfaces.

In order to evaluate the influence of various pump wavelengths on the measured barrier height V_B we display in Fig. 16 the PR spectra of the UN^+ sample at 300K in air for

λ_p = 633nm and 407nm taken with the same optical alignment. The penetration depth of these beams were 260nm (> L) for the former and 15.8nm (< L) for the latter [96]. Both pump beams had a photon flux (= $P_m/h\omega$) of 2 x 10^{13}photons-$s^{-1}cm^{-2}$. The two spectra have essentially identical FKO periods and hence the same V_S. The significance of this observation will be discussed below.

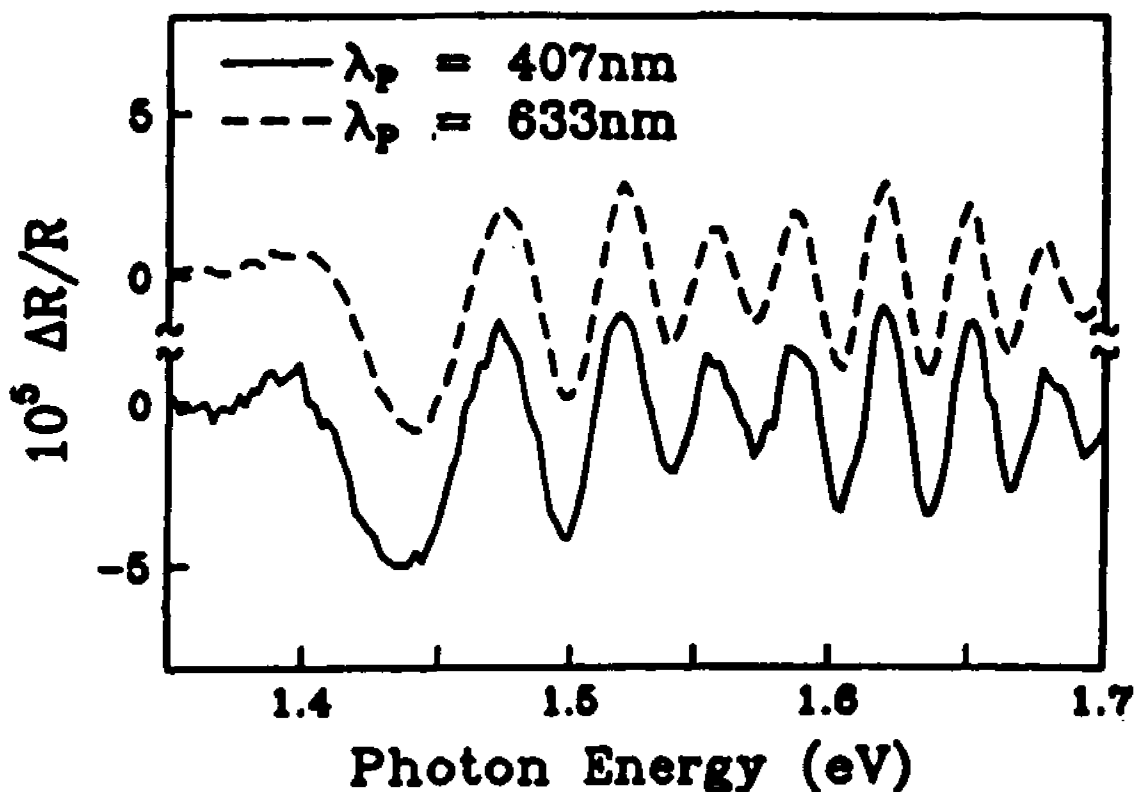

Figure 16. PR spectrum of the UN$^+$ sample at 300K (P_{pr} = 2 μW-cm^{-2}) with pump wavelengths of 633nm (dashed curve) and 407nm (solid curve). Both of the pump beams had a photon flux of 2 x 10^{13} photons $s^{-1}cm^{-2}$.

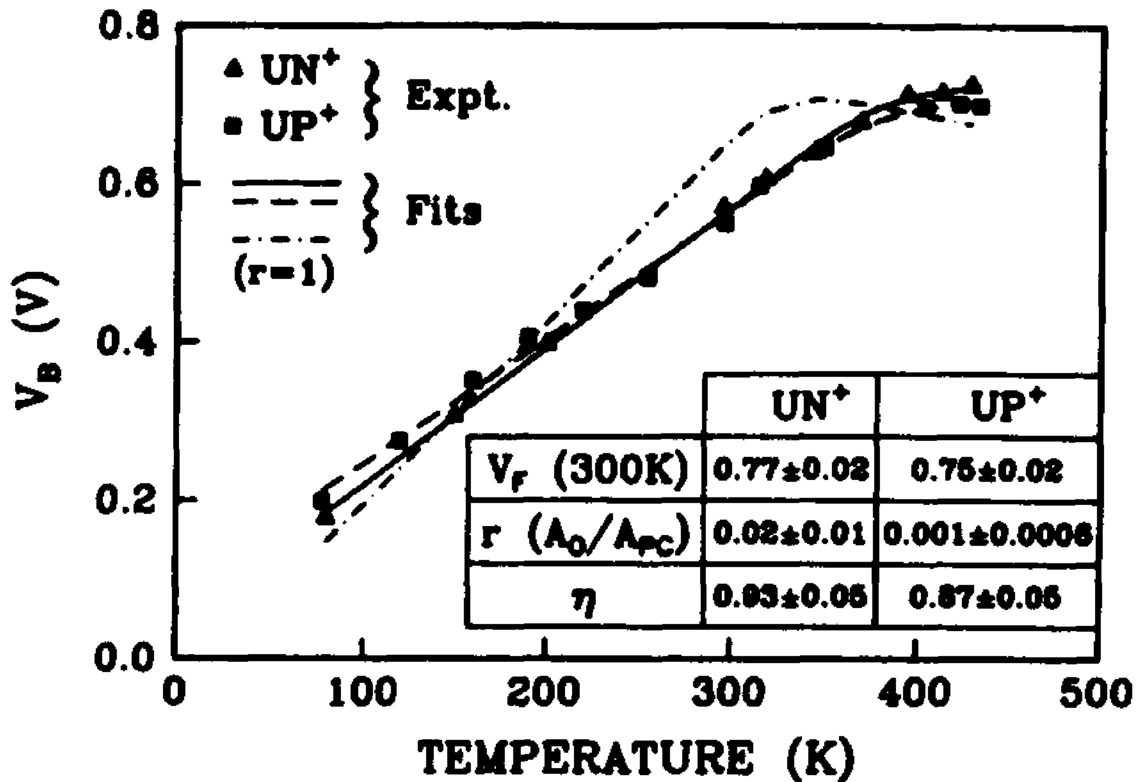

Figure 17. The measured barrier height V_B of the UN^+ (triangles) and the UP^+ (squares) samples as a function of temperature with P_{pu}= 3μW-cm^{-2} (633nm line) and P_{pr}= 2μW-cm^{-2}. The solid (UN^+) and dashed (UP^+) lines are least-squares fits to Eq. (29). The obtained values of $V_F(300)$, r and η are shown in the inset. $V_F(300)$ is in units of volts. The dot-dashed line is a least-squares fit (UN^+) to Eq.(29) for r= 1.

As demonstrated in Sec. 2.3, from the FKO observed in the PR spectra the built-in electric field and hence barrier height V_B can be accurately determined. Plotted in Fig. 17 are the values of V_B as a function of temperature for the UN^+

and UP^+ samples with P_{pu}=3μW-cm^{-2} (633nm line) and P_{pr}=2μW-cm^{-2}. We found no hysteresis of V_B with temperature cycling. In Fig. 17 V_B saturates at about 400K. At room temperature V_S (= V_F-V_B) is still an appreciable factor for these low light levels.

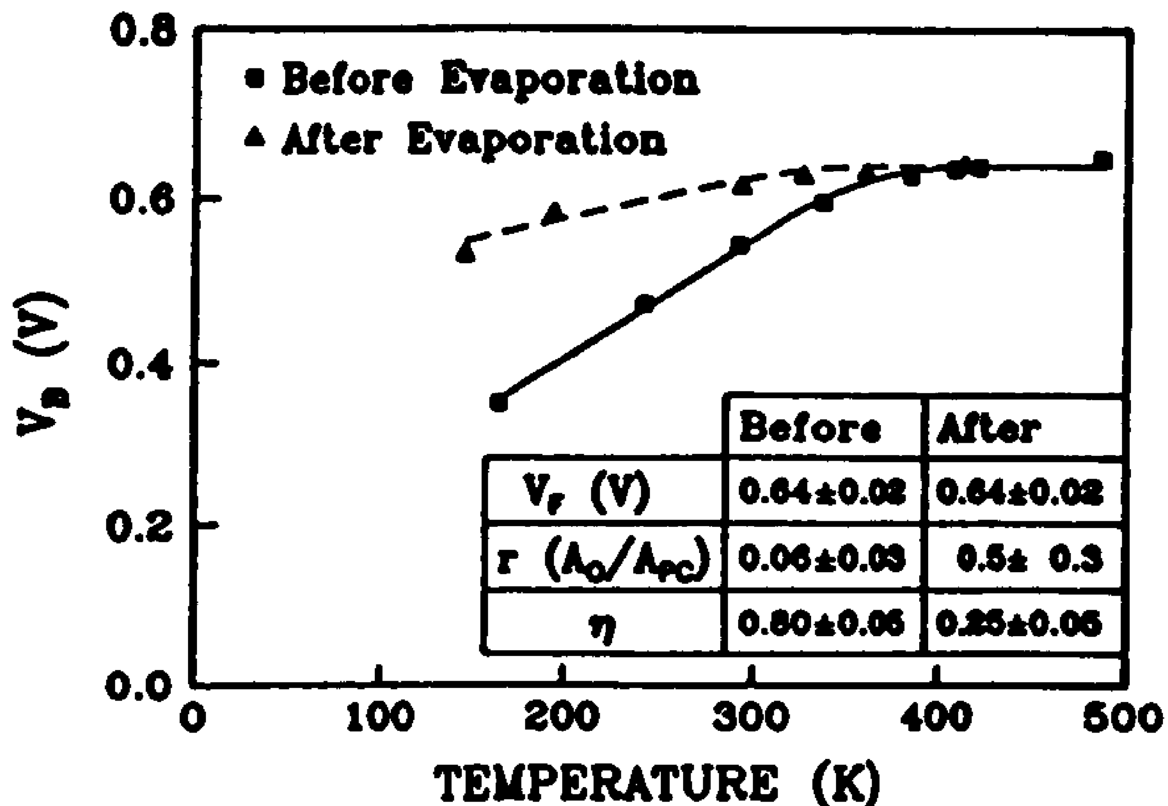

Figure 18. Values of V_B of the UN^+ sample in an ultra-high vacuum chamber, before and after 4 monolayer of W deposition, as a function of temperature with P_{pu} = 40μW-cm^{-2} (633nm line) and P_{pr} = 10μW-cm^{-2}. The solid (before evaporation) and dashed (after evaporation) lines are least-squares fits to Eq. (29). The obtained values of V_F(300), r and η are shown in the inset. V_F(300) is in units of volts.

After completing the measurements in air the UN^+ sample was placed in a UHV chamber. Fig. 18 displays V_B as a function of temperature before and after a deposition of four monolayers of W in UHV with P_{pu} = 40μW-cm^{-2} (633nm line) and P_{pr} = 10μW-cm^{-2}. The illuminated area is about the same as the W-metallization region so that the effect of surface current can be neglected. No attempt was made to clean the sample before metallization. Note that before metallization V_B saturates to a value of 0.70V in the UHV which is somewhat lower than 0.77V in air (see Fig. 17). After metallization V_B saturates at a lower temperature in relation to the bare surface. The limiting value of V_B did not change before and after metallization.

In addition, in order to explore surface photovoltage effects on the determination of Fermi level pinning, measurements were also carried out as a function of temperature (77K<T<450K) and light intensity of the pump (P_{pu}), probe (P_{pr}), and dc (P_{dc}) beams. The pumps beam was the 632.8nm line of a He-Ne laser. A second He-Ne laser was used to produce P_{dc}. Plotted in Fig. 19 are the values of V_B of the UN^+ sample (L=110nm) as a function of temperature for various of P_{pu}, P_{pr} and P_{dc}. For the lowest light intensity, V_B saturates at about 400K. Higher intensities decrease V_B (i.e., greater V_S) at a temperature and shift the saturation to higher temperatures.

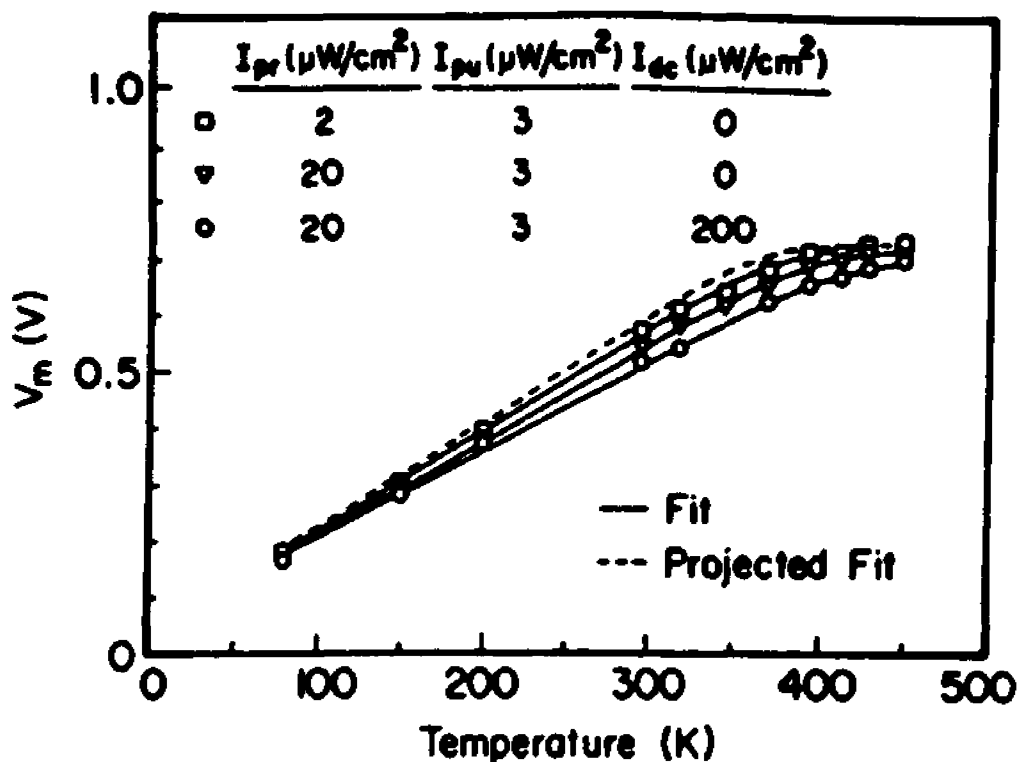

Figure 19. Measured barrier height V_B of the UN$^+$ sample as a function of temperature and light intensity. The solid lines are least-squares fits to Eq. (29). The dashed line is a generated curve corresponding to a light intensity of 0.4μW-cm^{-2}

3.1.2. Discussion

Based on current-transport theory V_S can be expressed as [45,97]:

$$V_S = (\eta kT/q)\ \ln(I_{pc}/I_o(T) + 1) \qquad (26)$$

where η is an ideality factor, I_{pc} is the photo-induced current and $I_o(T)$ is the saturation (dark) current which depends on the dominant current flow mechanism [45]. The quantity I_{pc} is equal to the photo-induced current density, J_{pc}, multiplied by the illuminated area, A_{pc}. On the other hand $I_o(T)$ is the saturation current density $J_o(T)$ times some effective area, A_o, which contributes to this current mechanism. For the sample configurations and temperature range of our experiment, thermionic-emission and diffusion are the main contributions to $J_o(T)$ so that we can write [45]:

$$J_o(T) = [A^*T^2/(1 + BT^{3/2})]\exp[-qV_F(T)/kT] \qquad (27a)$$

where

$$A^* = m^*qk^2/(2\pi^2h^3) \qquad (27b)$$

is the modified Richardson constant,

$$B = (k/2\pi m^*)^{1/2}(300/v_o) \qquad (27c)$$

and $V_F(T)$ is the temperature dependent Fermi level. We assume

that the temperature dependence of V_F is the same as that of the band gap and hence can be represented by the Varshni expression, i.e.[98]:

$$V_F(T) = V_F(300) - \alpha(T + 116)(T - 300)/(\beta + T) \qquad (27d)$$

where $V_F(300)$ is the Fermi level at 300K and α (= 5.1×10^{-4}V/K) and β (=190K) are the Varshni coefficients for GaAs [98]. In Eq. (27d) the reference temperature has been taken to be 300K, rather than the more common T = 0K value, since we are most interested in $V_F(300)$.

The quantity v_o is the saturation velocity at room temperature and is equal to 6×10^6cm-s^{-1} for electrons and 2×10^6cm-s^{-1} for heavy-holes [99]. We find for the UN$^+$ sample $A^* = 8.0$A-cm^{-2}K^{-2}, $B = 3.3\times10^{-4}$K$^{-3/2}$ and for the UP$^+$ sample $A^* = 54$A-cm^{-2} K^{-2} and $B = 4.9\times10^{-5}$K$^{-3/2}$ using effective masses of 0.067 for electron and 0.45 for heavy-hole (in units of free electron mass) [100].The heavy-hole mass is used because of its large density of states in relation to the light-hole.

Since J_{pc} consists of both drift and diffusion components, it can be written as [101]:

$$J_{pc}=qP_m\gamma(1-R_o)/h\omega \times \{[1-\exp(-\alpha W)] + \alpha L_d\exp(-\alpha W)/(1+\alpha L_d)\} \quad (28a)$$

where P_m is the light intensity, γ is quantum efficiency ($\approx$1), R_o is the reflectivity of the light at the semiconductor surface (=0.34) [96], $h\omega$ is the photon energy of the light, α is the absorption coefficient, W is the depletion width (to first order W is the undoped layer thickness L) and L_d is the diffusion length of the minority carriers. In the case when the diffusion length is much longer than the light penetration depth, i.e., $\alpha L_d >> 1$, Eq. (28a) becomes:

$$J_{pc} = qP_m\gamma(1-R_o)/h\omega \quad (28b)$$

In this situation, effectively all the charge carriers generated by the light contribute to J_{pc}.

This is indeed the case for our sample configurations as shown in Fig. 16. Pump beam wavelengths are such that the penetration depths of the light are both larger and smaller than L yielded the same result. This observation demonstrates that J_{pc} does not depend on α for our experiment and hence J_{pc} can be determined from P_m using Eq. (28b).

The expression for the temperature dependent barrier height, V_B, can be also written in terms of current densities

as [18,97]:

$$V_B = V_F(T) - (\eta kT/q)\ \ln\{[J_{pc}/rJ_o(T)] + 1\} \qquad (29a)$$

where the quantity r is:

$$r = A_o/A_{pc} \qquad (29b)$$

In Refs. 18 and 97 this factor was not used.

A one-dimensional transport equation is relevant for our work since the electric field is in the undoped top layer of the samples. A background doping level of 1×10^{14} cm^{-3} (generally p-type) would lead to a Debye length of about 0.4 microns. Thus, there is essentially no lateral variation of the potential.

From Eqs. (27a) and (29a), at sufficiently high temperature V_S becomes negligible because of the factor $\exp[-qV_F(T)/kT]$ and hence V_B approaches V_F. This is not the case in Ref. 18 since the unity term in the brackets of Eq. (29a) was omitted. The quantity J_{pc} can be calculated from Eq. (28b). For the light intensities used in Figs. 17 and 18 the corresponding J_{pc} were 2.2×10^{-6}A-cm^{-2} and 2.2×10^{-5}A-cm^{-2}. The corresponding J_{pc} for the light intensities used in Fig. 19 are listed in Table II.

By fitting the curves in Figs. 17, 18 and 19 to Eq.

(29a) the parameters $V_F(300)$, η and r can be obtained. The solid and dashed lines in Fig. 17 are least-squares fits of the experimental data to Eq. (29a) for the UN^+ and UP^+ structures, respectively, with $V_F(300)$, η and r as the variables. In order to demonstrate the necessity of including the geometry factor r, we display by the dot-dashed line in Fig. 17 the least-squares fit to the UN^+ data to Eq. (29a) for $r = 1$. As can be seen the agreement between the fit and experiment is not very good. The solid and dashed lines in Fig. 18 are least-squares fits of the data to Eq. (29a) for a UN^+ sample in UHV before and after evaporation of four monolayers of W, respectively.

In the insets of Figs. 17 and 18 we present the obtained values of $V_F(300)$, η and r. $V_F(300)$ is in units of volts. The Fermi pinning levels, V_F, of the UN^+ and UP^+ samples in the air approximately add up to the band gap of GaAs. This agrees with the complementary of the UN^+ and UP^+ structures in contrast to the results of Van Hoof et al [36] where the sum of their values of V_F was only half of the band gap. We believe that this deviation is due to photovoltaic effect which was not taken into account in their work. Recently, Sydor et al [102] have proposed an interpretation of the results of Ref. 36 based on a nonuniform field in the top undoped layer. Since 15 FKO

extrema have been detected in our structure (see Fig. 10) we feel that this is not the case in our experiment.

Even though we have no quantitative explanation for the difference in V_F in air and when placed in the UHV environment, the variation of surface potential, as characterized by photoluminescence, is well documented [103]. A reasonable speculation on this matter is that absorbed gases induce a fixed surface charge in the native oxide causing a shift in the measured GaAs surface potential. Since the GaAs surface is already "pinned" the W-metal deposition causes no change in V_F.

The solid lines in Fig. 19 are least-squares fits of the experimental data to Eq. (29a) for the UN^+ sample with $V_F(300)$, η and r as the variables. The fitting results are listed in Table II. The obtained values for different

Table II. Fit results of Fig. 19

J_{pc} (μA-cm^{-2})	$V_F(300)$ (V)	η	r (A_o/A_{pc})
2.2	0.77±0.02	0.93±0.05	0.02±0.01
22	0.77±0.02	0.93±0.05	0.02±0.01
220	0.77±0.03	0.92±0.05	0.04±0.03

light intensities are essentially the same except for the

highest light intensity case which has a higher r value with a larger error bar. The reason is probably due to the V_B still has not saturated at the highest temperature (450K, see Fig. 19). To illustrate the importance of V_S, at even low light levels, we have generated the dashed line in Fig. 19 which corresponds to a light intensity of 0.4μW-cm^{-2}. This result shows that, in order to get rid of VS, raising temperature is more efficient than reducing light intensity.

The parameter r in Eq. (29) is introduced as a geometric factor. It is based on the assumption that only a fraction of the surface has surface states [44]. The effective surface state area, A_o, contributes to the saturation current (= J_oA_o). However, the photo-induced current is equal to J_{pc} multiplied by the illumination area A_{pc}. Therefore r is the ratio of the surface state area to the illuminated area.

On a perfect (001) GaAs surface the atom density is 6.3×10^{14}cm^{-2}. Since r is the normalized surface state area then the density of the surface states (D_S), assuming one state per atom, is (6.3×10^{14})r cm^{-2}. From the values of r in the inset of Fig. 17 we have $D_S(n) = (1 \pm 0.6) \times 10^{13}$cm^{-2} for the UN$^+$ sample and $D_S(p) = (6 \pm 4) \times 10^{11}$cm^{-2} for the UP$^+$ sample. A possible speculation on the difference of the D_S for the UN$^+$ and the UP$^+$, as characterized by voltage-controlled photoetching [104], is that the depleted surface (the UP$^+$

case) has a smaller surface state density than the accumulated surface (the UN^+ case).

In the UHV environment for UN^+ the densities of the surface states are $D_S(n)=(2\pm1)\times10^{13}cm^{-2}$ before W-metallization and $D_S(n)=(4\pm3)\times10^{13}cm^{-2}$ after W-metallization. The effect of W-metal coverage is to increase the effective area of the surface states A_o (and hence r) and also to reduce the influence of V_S. Our results have shown this trend. The relatively large change in the ideality factor η after metallization is probably due to the leaking of surface charge to the metal clip used to hold the sample in place.

While the mechanism of PR as being due to the optical response of the material to the modulated surface electric field was established in early works [105] no quantitative connection between PR and the photovoltaic (PV) effect was made. Although several authors have compared PR and electroreflectance, no detailed theory relating PR and PV was presented [21,22]. The results of our experiment have established the detailed relation between the PR signal and V_S. Since PR can be performed over a wide temperature range we can get some information about the nature of the charge transfer process at the surface. To the best of our knowledge these are the first measured surface state density results on GaAs surface.

In conclusion, we have investigated the effects of V_S on V_B ($=V_F-V_S$) from (001) UN^+ and UP^+ GaAs structures with large, well controlled F as a function of T in the range 77K< T <450K. We have demonstrated that the dependence of V_B on T and light intensity P can be explained by a modified version of the theory of Hecht yielding values of $V_F = 0.77 \pm 0.02V$ for UN^+ and $V_F = 0.75 \pm 0.02V$ for UP^+ at 300K. These numbers approximately add up to the band gap of GaAs. This analysis also provides an experimental estimation of the densities of surface states on the GaAs surface. The influence of W-metal coverage (in-situ) is to increase the effective area of the surface states and hence to reduce the effect of V_S. The PR measurements with different pump wavelengths allowed us to accurately determine J_{pc}. Our analysis provides the quantitative relation between PR and the photovoltaic effect. The work presented here demonstrates the usefulness of PR, combined with these semiconductor structures, for the investigation of V_F and the nature of charge transfer mechanism.

3.2 In-Situ Photoreflectance Study of the Effects of Sputter/Annealing on the Fermi Level at (001) n- and p-Type GaAs Surfaces

As we have demonstrated earlier PR is a versatile tool which can accurately measure V_F in a variety of ambients and semiconductor interfaces e.g. vacuum, air,

metal/semiconductor, or semiconductor/semiconductor interfaces, etc. Using PR, one could monitor changes in V_F over a wide range of experimental conditions. This in turn could produce strong inferences concerning the fundamental mechanisms which determine V_F in a wide variety of non-ideal interfaces.

In this section we present a photoreflectance study of the effects of Ar^+ sputtering (500V) and thermal annealing (350°C) on the Fermi level, V_F, on the (001) UN^+ and UP^+ GaAs. The measurements were performed in-situ in an UHV chamber. Subsequent air exposure effects were also examined. The sample surfaces were monitored with Auger electron spectroscopy (AES) and high resolution low energy electron diffraction (LEED). Movement of V_F from midgap to near the conduction band, due to the sputtering, was found on both n- and p-type GaAs samples. The implication of these observations for various models of Schottky barrier formation will be discussed. The need to simultaneously measure both n- and p-type material in order to obtain unambiguous results will be also demonstrated.

3.2.1 Experimental Details and Results

The structures used in this study were the same as in Sec. 3.1.1, i.e., the UN^+ and UP^+ configurations. They were prepared by MBE by fabricating an undoped layer of thickness

L (= 110nm) on a buried 1μm Si-doped buffer ($n^+ \sim 2 \times 10^{18} cm^{-3}$) on an n^+ substrate and an undoped layer of L (= 220nm) on a 1μm Be-doped buffer ($p^+ \sim 1 \times 10^{18} cm^{-3}$) and p^+ substrate. In the PR measurements the pump beam was the 633nm line of a 5mW He-Ne laser chopped at 100Hz. A Perkin-elmer Phi 04-161 sputter ion gun was used in the Ar^+ sputtering study. The argon background pressure was 1×10^{-5}Torr. The Ar^+ energy of 500eV with emission current of 15mA, beam size of about 3mm in diameter and incident angle of about 80° were chosen to give a controllable, slow sputtering rate in order to have minimum lattice damage. The study of the Ar^+ sputtering (500V) and thermal annealing (350^oC) was performed in-situ in a UHV chamber with an operating pressure of better than 1.5×10^{-10} Torr. The surfaces were also monitored with Auger electron spectroscopy (AES) and high resolution LEED. The importance of simultaneously study both n-and p-type material will be discussed later.

Shown Fig. 20 are the effects of Ar-ion sputtering, thermal annealing and air exposure on V_B at 300K for the UN^+ [(V_B(n))] and UP^+ [V_B(p)] samples. Also displayed are the sum $V_B(n)+V_B(p)$ and E_g (=1.42eV), the band gap of GaAs. Light intensities of P_{pu} = 30μW-cm^{-2} and P_{pr} = 10μ W-cm^{-2} were used

in these measurements. Initially, on the undamaged surfaces the barrier height $V_B(n) = V_B(p)$ are at midgap. The quantity $V_B(n) + V_B(p)$ is only about 0.15eV below E_g. This small

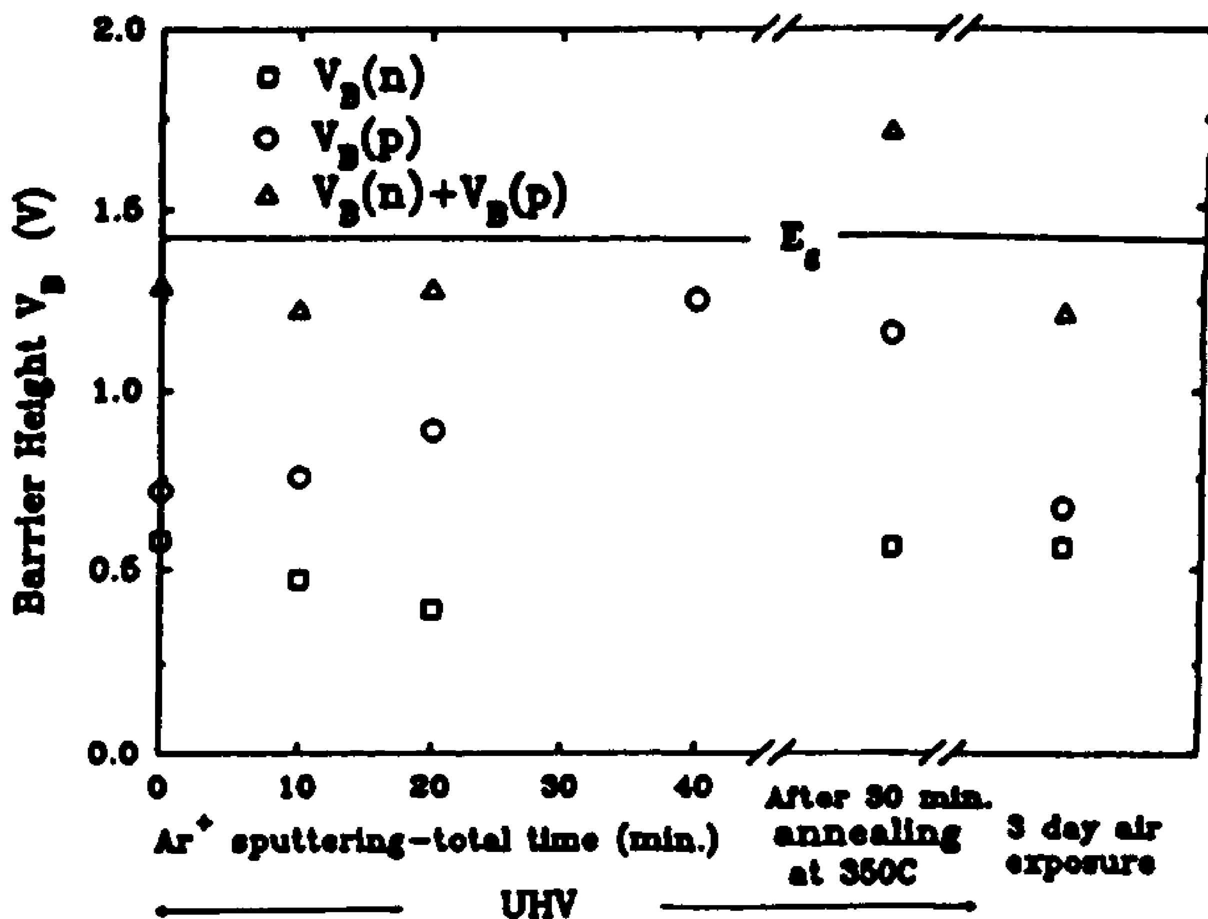

Figure 20. The measured barrier height V_B of the UN^+ (squares) and UP^+ (circles) samples as a function of Ar^+ sputtering time, thermal annealing and air exposure. the triangles are the sum of $V_B(n)+V_B(p)$. The band gap of GaAs, $E_g = 1.42$eV, also is denoted.

difference is probably due to the photovoltage effect [24-27]. With increasing sputtering time $V_B(n)$ decreases while $V_B(p)$ increases although $V_B(n) + V_B(p)$ remains approximately constant. After 40 minutes of sputtering no PR signal could obtained from the UN^+ sample which indicates that the built-in field and hence V_B (< 0.1V) is too small to observe. Therefore, $V_B(p)$ has a value approximately equal to that of $V_B(n) + V_B(p)$ for the previous conditions. These observations indicate that the major movement in V_B is due to changes in V_F not by differences in V_S. After 40 minutes of sputtering V_F has been moved from midgap to near the conduction band for both types of materials.

It is important to note that if only n-type material had been investigated the interpretation of the changes in $V_B(n)$ would have been ambiguous, e.g., was the decrease due to the unpinning of the surface or pinning at a position closer to the conduction band. The above observations clearly show the importance of simultaneously studying both n- and p-type systems.

Thermal annealing at 350°C for 30 minute in UHV reversed the movement of V_B and hence V_F. The parameter $V_B(n)$ went back to its original midgap value while $V_B(p)$ decreased but did not go back to its original position. About 3 days after the samples were removed from UHV chamber $V_B(p)$ went back to approximately its original midgap value and $V_B(n)$ remained

unchanged. These observations have considerable implication for the validity of various Schottky barrier models.

The surfaces were also monitored by AES and high resolution LEED. Before sputtering the AES shown that there were about 4 monolayers of oxygen and carbon on the surfaces which were probably due to the air exposure of the samples prior to the experiment. The LEED showed no clear diffraction spot because of the oxygen and carbon. As the sputtering time increased the oxygen and carbon decreased. After ten minutes of sputtering only one monolayer of oxygen and carbon were observed. Forty minutes of this procedure resulted in no detectable surface coverage. The surfaces still had no clear LEED pattern. This suggests that the surfaces were disordered by the sputtering. After the thermal annealing a clear zero-order LEED spot was observed indicating that order had been restored to the surface. However, since we cannot detect higher-order spots with the high resolution LEED, it was not possible to determine the detailed nature of the surface reconstruction.

3.2.2 Discussion

The results in Fig. 20 show conclusively that Ar^+ bombardment moves V_F from midgap and repins it near the conduction band for both UN^+ and UP^+ structures. Our observations cannot be explained by midgap models such as metal induced gap states (MIGS) [8-10], disorder induced gap

states (DIGS) [11] or the advanced unified defect model (ADM) [12,13]. If it turns out that the damage caused by the Ar^+ is insufficient to significantly perturb the bulk band structure near the surface, then these results would clearly rule out the importance of the MIGS model as the dominate physics in the Ar^+ treated surface. This is because the MIGS model puts V_F near midgap for GaAs. Even if the surface region is disordered by sputtering, as the LEED results suggest, the fact that the V_F moves close to the conduction band for both n- and p-type material also is in contradiction with the DIGS approach. The behavior of V_B (and hence V_F) illustrated in Fig. 20 does not, however, rule out the application of the effective work function (EWF) model [1,14] If the Ar^+ treatment generates a low work function phase, e.g. Ga, at the surface, the EWF model would predict V_F near the conduction band for both UN^+ and UP^+ structures. Of course these results could be due to new defects which have yet to be modeled. The important point is that the PR technique, combined with the UN^+ and UP^+ structures, supplies new and important information about Fermi level pinning at the surface. In addition, we have demonstrated the need to investigate both n- and p-type material in order to draw unambiguous conclusions about the influence of various surface treatments on V_F.

In conclusion, using PR we have studied the effects of Ar^+ sputtering and thermal annealing on V_F on (001) n- and p-type GaAs with large, uniform F. The measurements were performed in-situ in an ultrahigh vacuum chamber. The effect of the sputtering was to move V_F from midgap to near the conduction band for both types of materials. Subsequent UHV annealing (350°C) and air exposure restored V_F its original midgap value. These observations have considerable implications for various models of Schottky barrier formation. The movement of V_F with sputtering from midgap to near the conduction band, for both n- and p-type material, is inconsistent with midgap models such as MIGS, DISG or the ADM but could be explained by the EWF approach. This work also has shown the need to simultaneously measure both n- and p-type material in order to obtain unambiguous results.

3.3 Evolution of the Surface Voltage of Air Exposed MBE-Grown (001) GaAs

In order to explore the role of environment and V_S on the evaluation of V_F we have used PR to study the surface barrier height on the (001) MBE-grown UN^+ and UP^+ GaAs both in-situ in the MBE growth chamber and after exposure to air.

Shown by the solid and dashed lines in Fig. 21 are the PR spectra of the UN^+ (L=228nm) at 300K in the UHV MBE chamber and immediately after exposure to air, respectively,

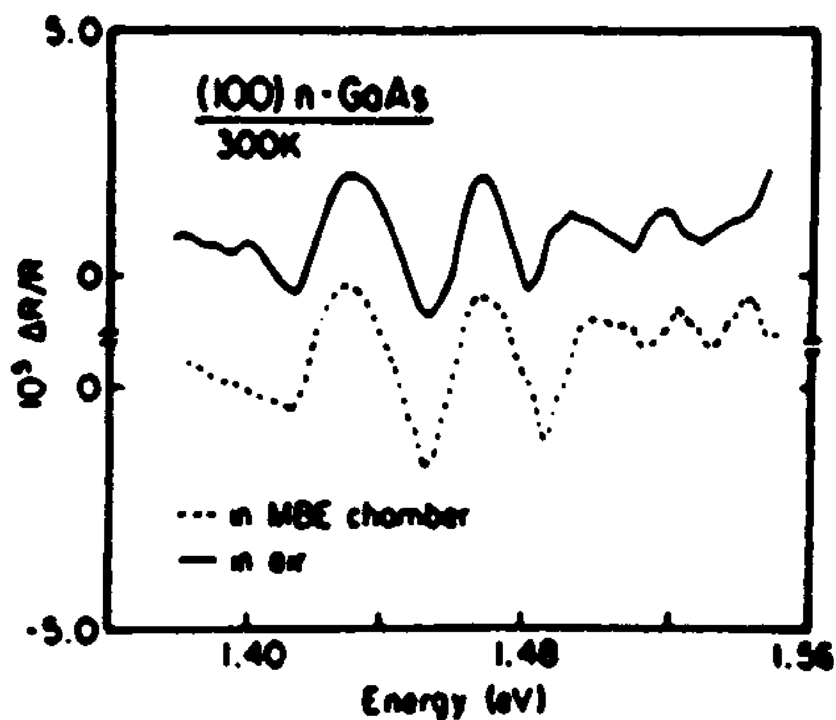

Figure 21. Photoreflectance spectra in MBE chamber and after exposure to air.

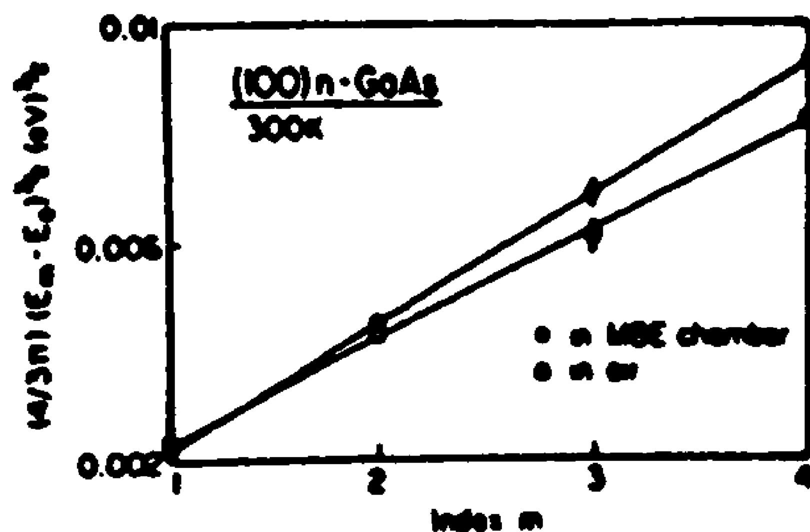

Figure 22. $(4/3\pi)(E_m-E_o)^{3/2}$ as a function of index m.

with P_{pu}=10μW-cm^{-2} and P_{pr}=2μW-cm^{-2}. Similar results were obtained for the UP$^+$ (L=228nm) sample. Shown in Fig. 22 is a plot of the FKO fit (see Sec. 2.3) from which the built-in field F can be determined.

From the above analysis, listed in Table III are the values of the measured barrier heights V_B for the the UN$^+$ and UP$^+$ samples in UHV and in air.There is a significant difference in surface potential between the UHV and air exposed surfaces. First we see that in UHV [$V_B(n)+V_B(p)$]=1.43eV, (the band gap energy for GaAs) and is greater than the sum of the n- and p-type surface potentials for air exposed surfaces (=1.23eV). Therefore, the air exposed surface is more "flat band" and hence less "pinned" than the UHV surface. We can understand this difference from the following considerations. In Ref. 15 it was shown that surface state density and hence "pinning intensity" is correlated with the degree of misorientation for (100)

Table III. THE MEASURED BARRIER HEIGHT FOR BOTH IN UHV AND IN AIR

	$V_B(n)$ (V)	$V_B(p)$ (V)
in UHV	0.69 ± 0.025	0.74 ± 0.035
in air	0.57 ± 0.025	0.66 ± 0.035

surfaces. This in turn correlates with atomic step density. Furthermore, Ref.15 showed that there is increased chemical reactivity at these atomic steps. If so, we might expect enhanced selective oxidation at atomic steps during air exposure. Therefore to explain the results of this work we surmise that in the UHV condition there is a maximum in surface state density due to "unpassivated" atomic steps. Air exposure causes preferential oxidation and hence passivation at the atomic steps. This in turn reduces the surface state density and hence the pinning density. Or, in the spirit of Sec. 3.1, less surface state density corresponds to smaller r factor and hence smaller V_B [see Eq. (29)].

In conclusion, from the FKO oscillations observed in the PR spectra of n- and p-type GaAs samples with well controlled built-in field we have investigated the effects of environment on the determination of V_F.

3.4. Nature of Band Bending at Semiconductor Surfaces by CER

In this Section we demonstrate that the CER can be used to evaluate the nature of band bending in a contactless manner. Results will be presented on different spectral features of bulk n- and p-type GaAs, semi-insulating (SI) GaAs, nominally undoped $In_{0.15}Ga_{0.85}As$, as well as the UN^+ and UP^+ GaAs and InP structures. The contactless determination of the character of band bending (and related

carrier type) has considerable ramifications. For example, it is often difficult to make the necessary contacts to samples for this assessment by traditional conductivity and Hall measurements. Also such experiments are difficult to interpret for the case of epitaxial layers fabricated on conducting substrates. Our technique will be compared to other contactless approaches for band bending determinations such as EBER [73,108], reflection difference spectroscopy (RDS) [107,108] and optically-induced electromagnetic radiation (OIEM) [109].

The n- and p-type bulk GaAs used in this study had carrier concentrations of $2x10^{17}cm^{-3}$ and $2x10cm^{-3}$, respectively, as determined from Hall measurements. The SI GaAs sample was Cr-doped Czrochalski grown material. The other samples investigated were prepared by molecular beam epitaxy. The undoped $In_{0.15}Ga_{0.85}As$ material was an epilayer of about 1μm in thickness grown on a (001) GaAs substrate. The undoped layer thicknesses L of the UN^+ and UP^+ structures used in the measurements were 228nm for GaAs and 100nm for InP. The CER apparatus has been described in Sec. 2.4.2. The modulating voltage was a square wave having 500V peak-to-peak at 80Hz. This value of the modulating voltage was sufficiently small so that all the measured lineshapes were independent of the modulating voltage.

Shown in Fig. 23 are the CER spectra at 300K in the

region of the direct band gap (E_o) from p-type GaAs (solid line), n-type GaAs (dotted line), SI GaAs (dashed line) and $In_{0.15}Ga_{0.85}As$ (dot-dashed line). The spectra are in the low-filed regime since the lineshape is independent of the magnitude of the modulating voltage and there are no FKO [67,69]. The In composition of the latter sample was determined from the relation [110] $E_o(In_xGa_{1-x}As) = E_o(GaAs) - 1.53x + 0.45x^2$. While all the lineshapes are fairly similar

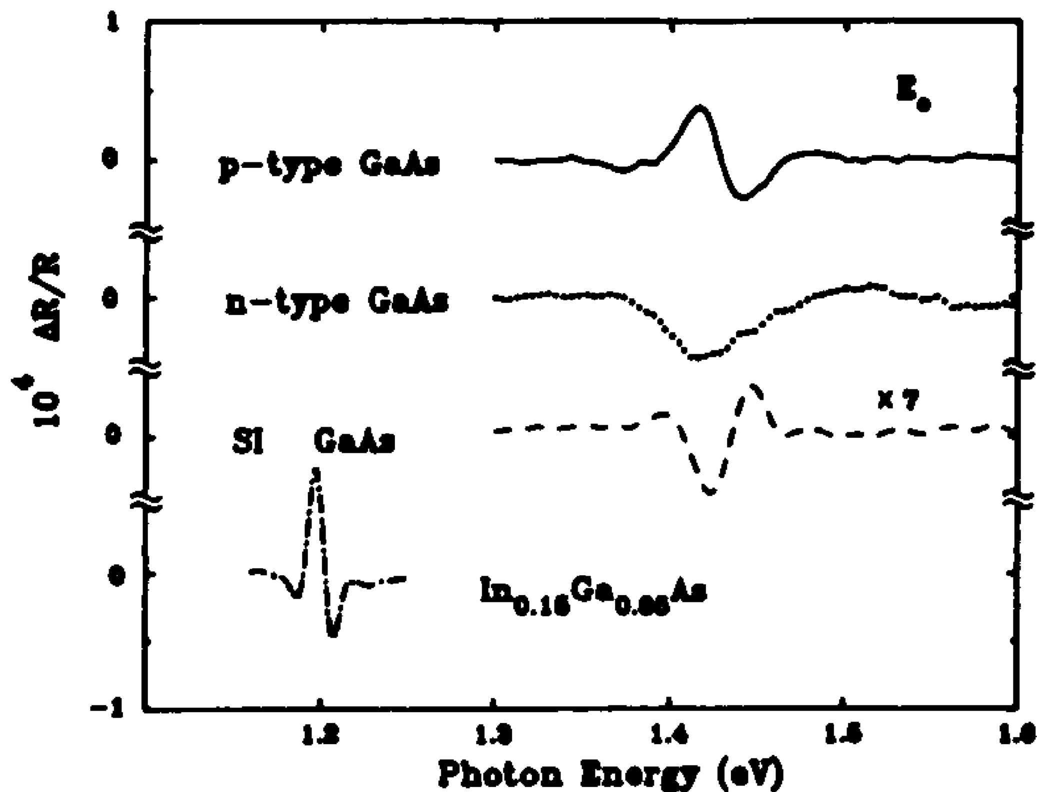

Figure 23. Contactless electroreflectance spectra at 300K in the region of E_o from p-type GaAs (solid line), n-type GaAs (dotted line), SI GaAs (dashed line) and nominally undoped $In_{0.15}Ga_{0.85}As$ (dot-dashed line).

there is a distant change in phase between the n- and p-type GaAs samples. The SI GaAs material has an n-type band bending while the $In_{0.15}Ga_{0.85}As$ has a p-type surface electric field. This latter observation is consistent for a p-type background doping level of about $5x10^{14}cm^{-3}$ in the MBE growth. The penetration depth of the light in the region of E_o is typically several thousand angstroms [111]

For GaAs these results are confirmed in Fig. 24 which displays the signals of the three samples in the region of

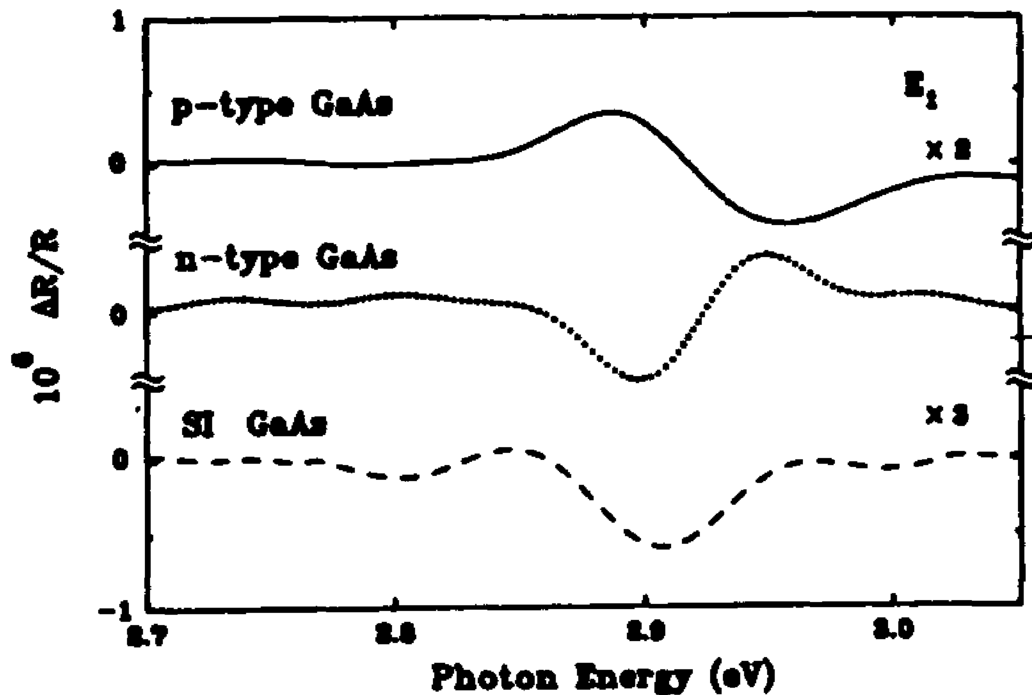

Figure 24. Contactless electroreflectance spectra at 300K in the region of E_1 from p-type GaAs (solid line), n-type GaAs (dotted line) and SI GaAs (dashed line).

the E_1 feature (Λ_3-Λ_1 transitions in the Brillouin zone) [67,68], Again there is a phase flip between the p- and n-type material and also the SI sample is n-type. The penetration depth of the light in the region of the E_1 resonance is typically several hundred angstroms [111].

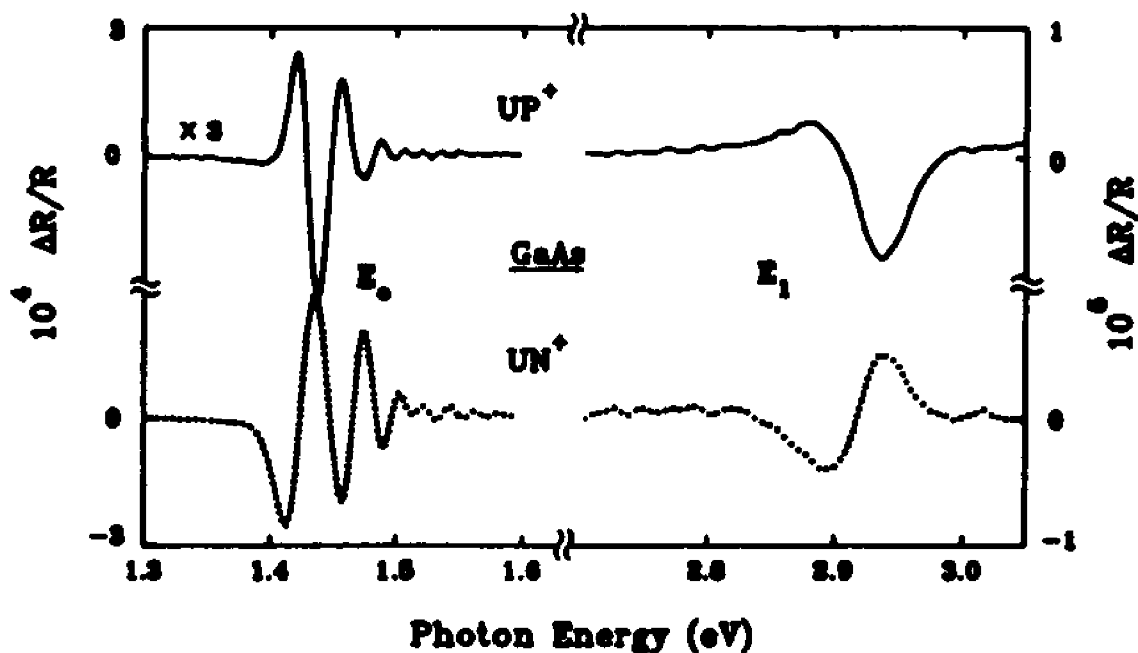

Figure 25. Contactless electroreflectance spectra at 300K in the region of E_o and E_1 transitions from UP^+ and UN^+ GaAs structures.

In Fig. 25 are displayed the CER spectra from the GaAs UP^+ and UN^+ samples at 300K in region of the E_o and E_1

features, respectively. Because of the large field (~2.5×10^4V/cm) the E_o signals display FKOs. The E_1 traces do not show FKOs since the broadening parameter Γ (~35meV) is larger than the electro-optic energy $\hbar\theta$ (~17meV). However, the most significant aspect of these spectra is the difference in phase between UP^+ and UN^+ materials for both E_o and E_1.

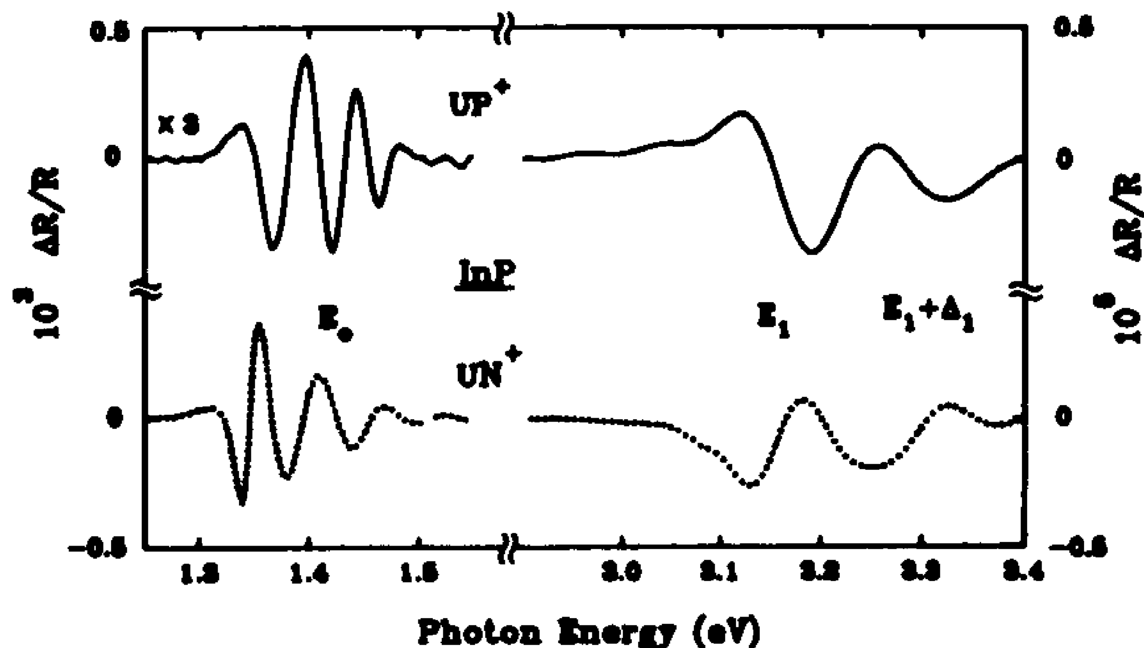

Figure 26. Contactless electroreflectance spectra at 300K in the region of E_o and E_1, $E_1 + \Delta_1$ transitions from UP^+ and UN^+ InP structures.

Similar results have been obtained for E_o, E_1 and $E_1 + \Delta_1$ of the InP UP^+ and UN^+ configurations as shown in Fig. 26 For E_o the two samples exhibit somewhat different periods for the FKOs probably due to the difference in Fermi level pinning on n- and p-type InP.

The reason for the phase change in electroreflectance (ER) associated with the nature of the band bending can be understood as follows. Consider n-GaAs, in which the bands are bent upward. If a modulating voltage is applied such that in the first (second) half-cycle V_{ac} increases (decreases) the surface field an ER signal of certain phase will be produced. However, in p-type material the first (second) half-cycle will decrease (increase) the field, thus leading to an opposite phase. Thus, flatband could be determine by observing the change in phase of ER signals. This property of ER has been known for many years [67,68,112] and is true whether the sample is in the low or intermediate (FKO) field regime [67]. In the past it has been used in contact modes to determine the nature of band bending including the evaluation of flatband [67,68,73,112]. In principle this method can be used on any crystallographic orientation. Photoreflectance signals do not have this phase information since the modulating light beam drives both n- and p-type material towards flatband.

Electron beam electroreflectance also could be used for

the band-bending evaluation [71]. However, to employ this method the sample must be placed in an UHV chamber. The RDS approach measures the polarization anisotropy of the near-normal reflectance of light linearly polarized along particular crystallographic directions, e.g., [110] and [110] in the plane of a (001) surface. To determine band bending this method takes advantage of the anisotropy produced by the linear electro-optic (LEO) effect. In the vicinity of the E_1 and $E_1 + \Delta_1$ features the LEO effect transfers oscillator strength from one transition to the other linearly in the space charge field normal to (001) or (110) surfaces [but not (111)]. There is no LEO effect for the E_o feature. Since the amplitude of the RDS signal is proportional to the surface field it also can be used as a measure of carrier concentration [107]. In OIEM a femtosecond laser beam illuminates a bare semiconductor surface creating electron-hole pairs. If there is a built-in field present, free carriers driven by the internal field are swept across the depletion layer and form a photocurrent normal to the surface. this transient photocurrent radiates a subpicosecond electromagnetic pulse with submillimeter wavelengths. thus OIEM yields information not only about the sign of the band bending but also field strength (doping concentration) and carrier mobility. However, it requires expensive, sophisticated equipment.

In conclusion we have demonstrated that CER, which

employs a simple capacitorlike arrangement, can conveniently be used to determine the sign of the surface band bending in semiconductors and semiconductor structures. Results have been obtained on n- and p-type GaAs, SI GaAs (n-type band bending), undoped $In_{0.15}Ga_{0.85}As$ (p-type) and n- and p-type GaAs and InP structures with large , almost constant electric fields. Thus this method is appropriate for either low or intermediate (FKO) field regimes.

3.5. A Electromodulation Study of GaAs with Excess Arsenic

The MBE growth of GaAs at temperature in the vicinity of 200°C results in GaAs with an arsenic rich stoichiometry in excess of 1%. In the as-growth conditions this excess arsenic correlates with a large arsenic antisite defect concentration [43]. When this material is annealed at about 600°C, the excess arsenic is converted into arsenic precipitates (GaAs:As) which have been shown to behave as buried Schottky barriers with a "pinned" barrier height of 0.7eV [44]. Less is known about the electrical behavior of the GaAs dominated by arsenic antisite defects.

We have used the PR and CER techniques to determine the electrical behavior of thin films of both types of GaAs with excess arsenic. The MBE grown structures used in this study were as follows: an N or P buffer layer with an undoped (U) layer followed by an as-grown low temperature layer (LT) or

an annealed LT (ALT) layer. Four different sequences were formed: LTUN, LTUP, ALTUN, and ALTUP. The key to the experiment is the fact that the electric field is non-zero and almost constant in the EM signals contains "useful" FKO from only the U regions of all samples. The FKO determines the electric field in the U region and, hence, the potential in the LT (ALT) region relative to the Fermi level in the N (P) region. Our results show that the Fermi level in the LT GaAs is 0.9eV above the valence band edge: whereas, the Fermi level in ALT GaAs (GaAS:As) is 0.7eV above the valence band edge.

CHAPTER IV

SUMMARY AND CONCLUSIONS

In this thesis we have used PR to study the surface barrier height on (001) MBE grown GaAs under a variety of conditions including air, ultrahigh-vacuum (UHV), sputter/annealing (in UHV), temperature (77K < T < 450K) in air and UHV, etc. Surface photovoltage (V_S) effects were evaluated as a function of temperature (77K < T < 450K), pump beam wavelength, W-metal coverage (in-situ) and light intensity. Our results have considerable implications for various models of Fermi level pinning and Schottky barrier formation.

The results of our experiment have established the detailed relation between the PR signal and V_S. In addition. The work presented in this thesis demonstrates the usefulness of PR, combined with the UN^+ and UP^+ structures, for the investigation of V_F and the nature of the charge transfer process.

We have developed a new contactless form of electromodulation which employs a capacitor-like system. It has several advantages over other contactless mode of EM. The utility of this approach has been demonstrated by measuring the CER spectra at 300K from a number of materials including SI bulk GaAs and bulk $Hg_{0.8}Cd_{0.2}Te$. The $Hg_{0.8}Cd_{0.2}Te$ results

are particularly significant since in the past it has not been able to obtain a contactless EM signal at 300K from this narrow gap material.

we have investigated the effects of V_S on V_B (= V_F-V_S) from (001) UN^+ and UP^+ GaAs structures with large, well controlled F as a function of T in the range 77K<T<450K. We have demonstrated that the dependence of V_B on T and light intensity P can be explained by a modified version of the theory of Hecht yielding values of V_F = 0.77 ± 0.02 V for UN^+ and V_F = 0.75 ± 0.02 V for UP^+ at 300K. These numbers approximately add up to the band gap of GaAs. This analysis also provides an experimental estimation of the densities of surface states on the GaAs surface. The influence of W-metal coverage (in-situ) is to increase the effective area of the surface states and hence to reduce the effect of V_S. The PR measurements with different pump wavelengths allowed us to accurately determine J_{pc}. Our analysis provides the quantitative relation between PR and the photovoltage effect.

Using PR we have studied the effects of Ar^+ sputtering and thermal annealing on V_F on (001) n- and p-type GaAs with large, uniform F. The measurements were performed in-situ in an ultrahigh vacuum chamber. The effect of the sputtering was to move V_F from midgap to near the conduction band for both types of materials. Subsequent UHV annealing (350°C) and air exposure restored V_F its original midgap value. These

observations have considerable implications for various models of Schottky barrier formation. The movement of V_F with sputtering from midgap to near the conduction band, for both n- and p-type material, is inconsistent with midgap models such as MIGS, DISG or the ADM but could be explained by the EWF approach. This work also has shown the need to simultaneously measure both n- and p-type material in order to obtain unambiguous results.

From the FKO oscillations observed in the PR spectra of n- and p-type GaAs samples with well controlled built-in field we have investigated the effects of environment on the determination of V_F. The air exposure tend to passivate the surface and hence increase the surface photovoltage effects.

we have demonstrated that CER can conveniently be used to determine the sign of the surface band bending in semiconductors and semiconductor structures. Results have been obtained on n- and p-type GaAs, SI GaAs (n-type band bending), undoped $In_{0.15}Ga_{0.85}As$ (p-type) and n- and p-type GaAs and InP structures with large , almost constant electric fields. Thus this method is appropriate for either low or intermediate (FKO) field regimes.

APPENDIX
PUBLICATIONS

1. X.Yin, F.H.Pollak,
"A novel contactless mode of electroreflectance"
Appl. Phys. Lett. 59, 2305 (1991).

2. X.Yin, H-M.Chen, F.H.Pollak, Y.Chan, P.A.Montano,
P.D.Kirchner, G.D.Pettit and J.M.Woodall,
"Photoreflectance study of the Fermi level at (001)
n- and p-type GaAs surfaces", to be published in
J. Vac. Sci. Technol. B.

3. X.Yin, H-M.Chen, F.H.Pollak, Y.Cao, P.A.Montano,
P.D.Kirchner, G.D.Pettit and J.M.Woodall,
"In-situ photoreflectance study of the effects of
sputter/annealing on the Fermi level at (001) n- and
p-type GaAs surfaces", J. Vac. Sci. Technol. B.9, 2114
(1991).

4. X.Yin, H-M.Chen, F.H.Pollak, Y.Chan P.A.Montano,
P.D.Kirchner, G.D.Pettit and J.M.Woodall,
"Photoreflectance study of surface photovoltage
effects at (100) GaAs surfaces/interfaces"
Appl. Phys. Lett., 58, 260, (1991).

5. X.Yin, H-M.Chen, Z.Hang, F.H.Pollak, A.C.Warren,
P.D.Kirchner, G.D.Pettit and J.M.Woodall,
"Evolution of surface photovoltage of air exposed MBE
(100) GaAs", Proceedings of the 20th International
Conference on The Physics of Semiconductors,
Thessoloniki, 1990, ed. by E.M.Anastassakis and
J.D.Joannopoulos (World Scientific, Singapore, 1990)
Vol. 1, 227 (1990).

6. X.Yin, F.H.Pollak, L.Pawlowicz, T.O'Neil and M.Hafizi
"Characterization of $GaAs/Ga_{1-x}Al_xAs$ heterojunction
bipolar transistor structures using photoreflectance"
Appl. Phys. Lett. 56, 1278, 1990.

7. B.T.McDermott, K.G.Reid, N.A.El-Masry, S.M.Bedair,
W.M.Duncan, X.Yin and F.H.Pollak,
"Atomic layer epitaxy of GaInP ordered alloy", Appl.
Phys. Lett. 56, 1172, 1990.

8. X.Yin, F.H.Pollak, L.Pawlowicz, T.O'Neil and M.Hafizi "Photoreflectance of $GaAs/Ga_{1-x}Al_xAs$ heterojunction bipolar transistor structures", Proceedings of the Society of Photo-Optical Instrumentation Engineers (SPIE, Bellingham,1990) 1286, 404 (1990).

9. M.Capizzi, C.Coluzza, P.Frankl, A.Frova, X.Yin, F.H.Pollak and R.N.Sacks, "Photoreflectance and photoluminescence study of defect passivation by hydrogen in GaAlAs/GaAs/GaAs heterostructures", Proceedings of the Society of Photo-Optical Instrumentation Engineers (SPIE, Bellingham,1990) 1286, 50 (1990).

10. X.Yin, F.H.Pollak, B.T.McDermott, K.G.Reid and S.M.Bedair, "Photoreflectance of a $GaAs/In_{0.5}Ga_{0.5}P$ (ordered) single quantum well grown by atomic layer epitaxy" MRS Symp. Proc. 160, 679, (1990).

11. B.T.McDermott, K.G.Reid, A.Dip, N.A.El-Masry, S.M.Bedair, W.M.Duncan, X.Yin and F.H.Pollak, "Ordered ternary alloys by atomic layer epitaxy", MRS Symp. Proc. 160, 365, (1990).

12. X.Yin, F.H.Pollak, J.T.Fitch, C.H.Bjorkman and G.Lucovsky, "Photoreflectance study of strain at Si/SiO_2 interfaces prepared by thermal oxidation of silicon", Proceedings of the Society of Photo-Optical Instrumentation Engineers (SPIE, Bellingham,1989), 1186, 122, (1989).

13. J.T.Fitch, C.H.Bjorkman, G.Lucovsky, F.H.Pollak and X.Yin, "Intrinsic stress and stress gradients at the SiO_2/Si interface in structures prepared by thermal oxidation of Si and subjected to rapid thermal annealing", J. Vac. Sci. Technol., B7, 775 (1989).

14. J.T.Fitch, C.H.Bjorkman, G.Lucovsky, F.H.Pollak and X.Yin, "Local atomic structure at thermally grown Si/SiO_2 interfaces", Appl. Surface Sci., 39, 103, (1989).

15. C.J.Wei and X.Yin,
"Experimental study of HEMT", J. Electronics, Sinica, Nov. 78, (1985).

16. X.Yin,
"Experimental study and computer simulation of transfered electron FET", M.S. degree thesis at Institute of Semiconductors, Academia, Sinica.

BIBLIOGRAPHY

1. See, for example, J. M. Woodall, P. D. Kirchner, J. L. Freeouf and A. C. Warren, Solid State Electronics, 33, 53 (1990) and reference therein.

2. See, for example, L. J. Brillson, Comments Cond. Mat. Phys., 14, No. 6, 311 (1989) and reference therein.

3. W. E. Spicer, Defects in III-V Compound Semiconductors, ed. by E. Weber, to be published by Academic Press.

4. K. Horn, Appl. Phys. A 51, 289 (1990).

5. J. R. Waldrop, J. Vac. Sci. Technol., B2(3), 445 (1984).

6. W. Schottky, Z. Phys. 118, 539 (1942).

7. J. Bardeen, Phys. Rev. 71, 717 (1947).

8. V. Heine, Phys. Rev. 138, A1689 (1965).

9. J. Tersoff, Phys. Rev. Lett., 32, 465 (1984).

10. S. G. Louie and M. L. Cohen, Phys. Rev.,B13, 2461 (1976)

11. H. Hasegawa and T. Sawada, Thin Solid Films 103, 119 (1983).

12. W. E. Spicer, I. Lindau, P. R. Skeath, C. Y. Su, and P. W. Chye, Phys. Rev. Lett., 44, 420 (1980).

13. R. F. Allen and J. D. Dow, Phys. Rev., B25, 1423 (1982).

14. J.L.Freeouf and J.M.Woodall, Appl. Phys. Lett., 39, 727 (1981).

15. S. Chang, L. J. Brillson, Y. J. Kime, D. S. Rioux, P. D. Kirchner, G. D. Pttit, J. M. Woodall and M. Hecht, Phys. Rev. Lett., 64, 2551 (1990)

16. S. P. Svensson, J. Kanski, T. G. Anderson, and P. O. Nilsson, J.Vac. Sci. Technol. B2 335 (1981).

17. L. A. Farrow, C. J. Sandroff and M. C. Tamargo, Appl. Phys. Lett., 51, 1931 (1987).

18. M. Hecht, Phys. Rev., B41, 7918 (1990); also, J. Vac. Sci. Technol., B8(4), 1018 (1990).

19. K. Jacobi, U. Myler and P. Althainz, Phys. Rev., B41, 10721 (1990).

20. S. Chang, I. M. Vitomirov, L. J. Brillson, Y. J. Kime, D. S. Rioux, P. D. Kirchner, G. D. Pettit, J. M. Woodall and M. Hecht, Phys. Rev. B41, 12299 (1990)

21. R. N. Battacharya, H. Shen, P. Parayanthal, F.H. Pollak, T. Coutts and H. Aharoni, Phys. Rev. B37, 4044 (1988); also, Proceedings of the Society of Photo-Optical Instrumentation Engineers (SPIE, Bellingham,1987) 794, 81 (1987), also, Solar Cells 21, 371 (1987).

22. R. Glosser and N. Bottka in the Proceedings of the Society of Photo-Optical Instrumentation Engineers (SPIE, Bellingham,1987) 794, 88 (1987).

23. H. Shen, F. H. Pollak, J. M. Woodall, J. Vac. Sci. Technol., B8, 413 (1990).

24. H. Shen, M. Dutta, L. Fotiadis, P. G. Newman, R. P. Moerkirk, W. H. Chang and R. N. Sacks, Appl. Phys. Lett., 57, 2118 (1990).

25. X. Yin, H-M. Chen, F. H. Pollak, Y. Chan, P. A. Montano, P. D. Kirchner, G. D. Pettit and J. M. Woodall, Appl. Phys. Lett., 58, 260, (1991).

26. X. Yin, H-M. Chen, Z. Hang, F. H. Pollak, A. C. Warren, P. D. Kirchner, G. D. Pettit and J. M. Woodall, Proc. of 20th Int. Conf. on The Physics of Semiconductors ed. by E. M. Anastassakis and J. D. Joannopoulos (World Scientific, Singapore, 1990), Vol. 1, 227.

27. X. Yin, H-M. Chen, F. H. Pollak, Y. Chan, P. A. Montano, P. D. Kirchner, G. D. Pettit and J. M. Woodall, to be published in J. Vac. Sci. Technl., B

28. H. Shen, P. Parayanthal, F. H. Pollak, R. N. Sacks and G. Hickman, Proceedings of the Society of Photo-Optical Instrumentation Engineers (SPIE, Bellingham, 1987) 794, 88 (1987).

29. R. A. Street, R. H. Williams, and R. S. Bauer, J. Vac. Sci. Technol., B17, 1001 (1980).

30. J. Y. Duboz, P. A. Badoz, F. Arnaud d'Avitaya and E. Rosencher, Phys. Rev. B40, 10609 (1989).

31. N. Bottka, D. K. Gaskill, R. S. Sillmon, R. Henry and R. Glosser, J. Electron Mater., 17, 161 (1988)

32. F. H. Pollak and H. Shen, in Proceedings of the Society of Photo-Optical Instrumentation Engineers (SPIE, Bellingham,1989) 1037, 16 (1989).

33. R. Enderlein, in Proceedings of the Society of Photo-Optical Instrumentation Engineers (SPIE, Bellingham,1990) 1286, 188 (1990).

34. X. Yin and F. H. Pollak, Appl. Phys. Lett., 59, 2305 (1991).

35. X. Yin, H-M. Chen, F. H. Pollak, Y. Cao, P. A. Montano, P. D. Kirchner, G. D. Pettit and J. M. Woodall, J. Vac. Sci. Technl., B9, 2114 (1991)

36. C. Van Hoof, K. Deneffe, J. DeBoeck, D. J. Arent and G. Borghs, Appl. Phys. Lett., 54, 608 (1989).

37. A. Y. Cho, J. Appl. Phys., 47, 2841 (1976).

38. R. Z. Bachrach, Prog. Crys. Growth Charact. 2, 115 (1979).

39. R. Z. Bachrach, R. S. Bauer, G. V. Hansson, and P. Chiaradia, J. Vac. Sci. Technol. 18, 797 (1981).

40. R. E. Viturro, J. L. Shaw, C. Mailhiot, N. Tache, J. McKinley, G. Margaritondo, J. M. Woodall, P. D. Kirchner, G. D. Pettit, S. L. Wright and L. J. Brillson, Appl. Phys. Lett., 52, 2052 (1988).

41. Z. Lilienthal-Weber, R. Gronsky, J. Wahburn, N. Newman, W. E. Spicer and E. R. Weber, J. Vac. Sci. Technol. B4, 912 (1986).

42. F. W. Smith, A. R. Calawa, Change-Lee Chen, M. J. Mantra, and L. J. Mahoney, IEEE Electron

Device Lett. 9, 77 (1988).

43. M. Kaminska, Z. Liliental-Weber, E. R. Weber, T. George, J. B. Kortright, F. W. Smith, B-Y. Tsaur, and A. R. Calawa, Appl. Phys. Lett. 54, 1881 (1989).

44. A. C. Warren, J. M. Woodall, J. L. Freeouf, D. Grischkowsky, D. T. McInturff, M. R. Melloch and N. Otsuka, Appl. Phys. Lett., 57, 1331 (1990).

45. E. H. Rhoderick, in Metal-Semiconductor Contacts (Clarendon Press, Oxford, 1980).

46. J. M. Woodall, N. Braslau, and J.L. Freeouf, in Physics of Thin Films: Advances in Research and Development, Vol. 13, edited by A. Erancombe and J. Vossen (Academic Press, New York, 1987) p.199.

47. R. Z. Barchrach, in Metal-Semiconductor Schottky Barrier Junctions and Their Applications, edited. by B. L. Sharma (Plenum Press, New York, 1984) p.61.

48. W. E. Spicer, N. Newman, T. Kendelewicz, W. G. Petro, M. D. William, C. E. McCants, and I. Lindau, J. Vac. Sci. Technol., B3, 117 (1985).

49. C. B. Duke, R. J. Meyer, and P. Mark, J. Vac. Sci. Technol. 17, 971 (1980).

50. D. J. Chadi, Phys. Rev. B19, 2074 (1979).

51. A. Huijser and J. van Laar, Surf.Sci. 52, 202(1975)

52. N. F. Mott, Proc. Camb. Phil. Soc. 34, 568 (1938).

53. R. L. Farrow, R. K. Chang, S. Mroczkowski and F. H. Pollak, Appl. Phys. Lett. 31, 768 (1977).

54. G. P. Schwartz, G. J. Gaultieri, J. E. Griffiths, C. D. Thurmond and B. Schwartz, J. Electrochem. Soc. 127, 2488 (1980).

55. H. H. Wielder, J. Vac. Sci. Technol. 15, 1498 (1978)

56. A. Hiraki, K. Shuto, S. Kim, W. Kammura and M. Iwami Appl. Phys. Lett. 31, 611 (1977).

57. J. L. Freeouf and J. M. Woodall, Surf. Sci. 168, 518 (1986).

58. I. Tamm, Phys. Zeits. Sowjetunion, 1, 733 (1932).

59. P. W. Chye, L. A. Babalola, T. Sukegawa and W. E. Spicer Phys. Rev. Lett., 35, 1602 (1975).

60. F. Flores and C. Tejedor, J. Phys. C: Solid State Physics 20, 145 (1987).

61. E. R. Weber, H. Ennen, V. Kaufmann, J. Windschief, J. Schneider and T. Wosinski, J. Appl. Phys. 53, 6140 (1982).

62. A. Zur, T. C. McGill and D. L. Smith, Phys. Rev. B28, 2060 (1983).

63. L. J. Brillson, Surf. Sci. Repts. 2, 123 (1982) and references therein; also L. J. Brillson, Phys. Rev. Lett. 40, 260 (1978).

64. L. J. Brillson, G. Margaritondo and N. G. Stoffel, Phys. Rev. Lett. 44, 667 (1980).

65. L. J. Brillson, C. F. Brucker, A. D. Katnani, N. G. Stoffel and G. Margaritondo, Phys. Rev. Lett. 46, 838 (1981).

66. M. Cardona, Modulation Spectroscopy, (Academic Press, New York, 1969) and references therein.

67. D. E. Aspnes in Handbook in Semiconductors, Vol.2, edited by M. Balkanski (North Holland, Amsterdam, 1980) p.109 and references therein.

68. F. H. Pollak, in Proceedings of the Society of Photo-Optical Instrumentation Engineers (SPIE, Bellingham,1981) 276, 142 (1981) and references therein.

69. F. H. Pollak, to be published in Handbook on Semiconductors, edited by M. Balkanski, and references therein.

70. Y. Hamakawa and T. Nishino in Optical Properties of Solids: New Developments, edited by B. O. Seraphin

(North Holland, New York, 1976) p.225

71. W. E. Engeler, H. Fritzsche, M. Garfinkel, and J. J. Tiemann, Phys. Rev. Lett. 14, 1069 (1965).

72. B. Batz, Solid State Comm. 4, 241 (1965).

73. M. H. Herman, Proceedings of the Society of Photo-Optical Instrumentation Engineers (SPIE, Bellingham, 1990) 1286, 39 (1990).

74. F. H. Pollak and O. J. Glembocki, Proceedings of the Society of Photo-Optical Instrumentation Engineers (SPIE, Bellingham, 1988) 946, 2 (1988).

75. D. E. Aspnes, Surf. Sci. 37, 418 (1973).

76. Y. Yin, D. Yan, F. H. Pollak, G. D. Pettit and J. M. Woodall, Phys. Rev. B43, 12138 (1991).

77. D. E. Aspnes, Phys. Rev. B10, 4228 (1974).

78. H. Shen and F. H. Pollak, Phys. Rev. B42, 7097 (1990).

79. D. E. Aspnes and A. A. Stundna, Phys. Rev. B7, 4605 (1973).

80. B. V. Shanabrook and O. J. Glembocki, Proc. 18th Int. Cof. Phys. Semicond., Stockholm, edited by O. Engstrom (World Scientific, Singapore) p.565 (1987).

81. B. V. Shanabrook, O. J. Glembocki and W. T. Beard Phys. Rev. B35, 2540 (1987).

82. O. J. Glembocki and B. V. Shanabrook, Superlattices and Microstructures, 3, 235 (1987).

83. O. J. Glembocki and B. V. Shanabrook, Superlattices and Microstructures, 5, 603 (1989).

84. O. J. Glembocki, Proceedings of the Society of Photo-Optical Instrumentation Engineers (SPIE, Bellingham, 1990) 1286, 2 (1990).

85. D. S. Jiang, Y. S. Tang, J. B. Xia and R. Enderlein, Superlattices and Microstructures, 6, 387 (1989).

86. Y. S. Tang, J. Appl. Phys. 69, 8298 (1991).

87. O. J. Glembocki and B. V. Shanabrook, Semiconductors and Semimetals, Vol. 67, edited by D. Seiler (Academic Press, New York, 1992) p. XX.

88. Y. S. Haung, H. Qiang, F. H. Pollak, J. Lee and B. Elman, J. Appl. Phys. 70, XX (1991).

89. J. W. Garland, H. Abad, M. Viccaro and P. M. Raccah, Appl. Phys. Lett. 52, 1176 (1988).

90. X. L. Zheng, D. Heiman, B. Lax, F. A. Chambers and K. A. Stair, Appl. Phys. Lett. 52, 984 (1988).

91. W. M. Theis, G. D. Sanders, C. E. Leak, K. K. Bajaj and H. Morkoc, 1988, Phys. Rev. B37, 3042 (1988).

92. O. J. Glembocki and B. V. Shanabrook, Proceedings of the Society of Photo-Optical Instrumentation Engineers (SPIE, Bellingham, 1987) 794, 74 (1987).

93. H. Shen and M. Dutta, Appl. Phys. Lett. 57, 587 (1990).

94. M. Sydor, A. Badakhshan and J. R. Engholm, Appl. Phys. Lett. 58, 948 (1991).

95. A. Ksendzov, F. H. Pollak, P. M. Armitharaj and J. A. Wilson, J. Cryst. Growth 86, 586 (1988).

96. D. E. Aspnes, S. M. Kelso, R. A. Logan and R. Bhat, J. Appl. Phys. 60(2), 754 (1986).

97. H. Hovel, in Semiconductors and Semimetals, Vol. 11, (Academic, New York, 1975), p.59.

98. H. Shen, S. H. Pan, Z. Hang, J. Leng, F. H. Pollak, J. M. Woodall and R. N. Sacks, Appl. Phys. Lett. 53, 1080 (1988).

99. See, for example, S. M. Sze, Physics of Semiconductor Devices, 2nd ed., (Wiley, New York, 1981), p.46.

100. The effective masses used were taken from Landolt-Bornstein, Numerical Data and Functional Relationships in Science and Technology, ed. by O. Madelung, M. Schulz and H. Weiss (Spinger, New York, 1972) Vol. III/17b.

101. T. Kanata, M. Matsunaga, H. Takakura, Y. Hamakawa, and T. Nishino, in Proceedings of the Society of Photo-Optical Instrumentation Engineers (SPIE, Bellingham, 1990) 1286, 56 (1990).

102. M. Sydor, J. R. Engholm, M. O. Manesreh, C. E. Stutz, L. Liou and K. R. Evans, Appl. Phys. Lett. 56, 1769 (1990).

103. C. W. Wilmsen, P. D. Kirchner and J. M. Woodall, J. Appl. Phys. 64, 3287 (1988).

104. H. J. Hoffmann, J. M. Woodall and T. I. Chappell, Appl. Phys. Lett. 38, 564 (1981).

105. J. L. Shay, Phys. Rev. B2, 803 (1970).

106. P. M. Raccah, J. W. Garland, S. E. Buttrell, Jr., L. Francke and J. Jackson, Appl. Phys. Lett. 52, 1584 (1988).

107. S. E. Acosta-Ortiz and A. Lastras-Martinez, SPIE Proc. 1286, 31, (1990).

108. H. H. Farrel, M. C. Tamargo, T. J. Gmitter, A. L. Weaver and D. E. Aspnes, J. Appl. Phys. 70, 1033 (1991).

109. X.-C. Zhang, J. T. Darrow, B. B. Hu, D. H. Austin, M. T. Schmidt, P. Thorn and E. S. Yang, Appl. Phys. Lett., 56, 2228 (1990).

110. S. Adachi, J. Appl. Phys. 58, R1 (1985).

111. B. O. Seraphin and H. E. Bennet in Semiconductors and Semimetals, Vol. 3, ed. by R. K. Willardson and A. C. Beer (Academic, New York, 1967) p.499.

112. See, for example, P. Lemasson and C. Nguyen Van Huong, J. Electrochem. Soc. 135, 2080 (1988) and references therein.